






Article

Nanoparticles of Mixed-Valence Oxides $Mn_xCO_{3-x}O_4$ ($0 \leq x \leq 1$) Obtained with Agar-Agar from Red Algae (Rhodophyta) for Oxygen Evolution Reaction

Jakeline Raiane D. Santos ^{1,*}, Rafael A. Raimundo ², Thayse R. Silva ³, Vinícius D. Silva ³, Daniel A. Macedo ³, Francisco J. A. Loureiro ⁴, Marco A. M. Torres ¹, Domenica Tonelli ⁵ and Uílame U. Gomes ^{1,*}

¹ Materials Science and Engineering Postgraduate Program, UFRN, Natal 59078-970, Brazil

² Department of Physics, UFPB, João Pessoa 58051-900, Brazil

³ Materials Science and Engineering Postgraduate Program, UFPB, João Pessoa 58051-900, Brazil

⁴ Centre for Mechanical Technology and Automation, Mechanical Engineering Department, UA, 3810-193 Aveiro, Portugal

⁵ Department of Industrial Chemistry "Toso Montanari", Industrial Chemistry, UNIBO, V.le Risorgimento 4, 40136 Bologna, Italy

* Correspondence: jakelineedm@gmail.com (J.R.D.S.); umbelino@fisica.ufrn.br (U.U.G.)



Citation: Santos, J.R.D.; Alexandre, R.R.; Silva, T.R.; Silva, V.D.; Macedo, D.A.; Loureiro, F.J.A.; Torres, M.A.M.; Tonelli, D.; Gomes, U.U. Nanoparticles of Mixed-Valence Oxides $Mn_xCO_{3-x}O_4$ ($0 \leq x \leq 1$) Obtained with Agar-Agar from Red Algae (Rhodophyta) for Oxygen Evolution Reaction. *Nanomaterials* **2022**, *12*, 3170. <https://doi.org/10.3390/nano12183170>

Academic Editor: Ioannis V. Yentekakis

Received: 8 August 2022

Accepted: 7 September 2022

Published: 13 September 2022

Publisher's Note: MDPI stays neutral with regard to jurisdictional claims in published maps and institutional affiliations.



Copyright: © 2022 by the authors. Licensee MDPI, Basel, Switzerland. This article is an open access article distributed under the terms and conditions of the Creative Commons Attribution (CC BY) license (<https://creativecommons.org/licenses/by/4.0/>).

Abstract: The development of efficient electrocatalysts for the oxygen evolution reaction (OER) is of paramount importance in sustainable water-splitting technology for hydrogen production. In this context, this work reports mixed-valence oxide samples of the $Mn_xCO_{3-x}O_4$ type ($0 \leq x \leq 1$) synthesized for the first time by the proteic sol-gel method using Agar-Agar as a polymerizing agent. The powders were calcined at 1173 K, characterized by FESEM, XRD, RAMAN, UV-Vis, FT-IR, VSM, and XPS analyses, and were investigated as electrocatalysts for the oxygen evolution reaction (OER). Through XRD analysis, it was observed that the pure cubic phase was obtained for all samples. The presence of Co^{3+} , Co^{2+} , Mn^{2+} , Mn^{3+} , and Mn^{4+} was confirmed by X-ray spectroscopy (XPS). Regarding the magnetic measurements, a paramagnetic behavior at 300 K was observed for all samples. As far as OER is concerned, it was investigated in an alkaline medium, where the best overpotential of 299 mV vs. RHE was observed for the sample ($MnCo_2O_4$), which is a lower value than those of noble metal electrocatalysts in the literature, together with a Tafel slope of 52 mV dec⁻¹, and excellent electrochemical stability for 15 h. Therefore, the green synthesis method presented in this work showed great potential for obtaining electrocatalysts used in the oxygen evolution reaction for water splitting.

Keywords: electrocatalyst; green synthesis; proteic sol-gel; mixed-valence oxides

1. Introduction

In recent decades, with the exponential growth of the population, the intensification of using fossil fuels has generated great impacts on the environment [1]. Given this, the energy transition from fossil fuels to clean energy sources has become necessary, and major renewable energy technologies have been developed [2], such as geothermal [3], wind [4], solar [5,6], and biomass [7]. However, to benefit resources even more, it is necessary to use efficient devices for energy storage and conversion [8,9].

One of the energy conversion processes that has received a lot of attention is water splitting via electrolysis for the production of hydrogen [10], which consists of two semi-reactions: the hydrogen evolution reaction (HER) [11] and the oxygen evolution reaction (OER) [12–14]. During the water-splitting process, the kinetic reaction that takes place at the anode (OER) is slow and requires high energy consumption (overpotential) due to the four electrons transferred in the reaction, causing its efficiency to decrease [15]. Therefore,

the use of effective electrocatalysts is necessary to accelerate the reaction and reduce the overpotential [16]. However, the most widely used and effective electrocatalysts for water splitting are compounds based on noble metals such as ruthenium and iridium, but the high cost and scarcity of these elements have limited their large-scale application [17,18]. Therefore, one of the main challenges is to develop new electrocatalysts made of low-cost and abundant materials while also offering high electrochemical performance [19].

In this context, mixed-valence transition metal oxides such as the $Mn_xCo_{3-x}O_4$ (Mn-Co-O) system have attracted attention, as they represent an important class of multifunctional materials for electrocatalysis [20], oxygen evolution reaction [21], oxygen reduction reaction [22], fuel cells [23], and batteries [24]. These applications are related to the intrinsic properties of Mn-Co-O due to the multiple oxidation states of the metal ions [25]. This material has a spinel-like structure, with general formula $A[B]_2O_4$, where A is represented by a cation in the tetrahedral site (Coordination Number 4), and B is a cation in the octahedral site (Coordination Number 6) [26]. Depending on the occupancy of the divalent (A) and trivalent (B) cations, spinels are classified into three categories, normal, inverse, and complex [27], which gives them interesting physical, chemical [28], and electrochemical properties [29].

Furthermore, the distribution of cations between the different coordination sites strongly depends on the synthesis conditions [30]; thus, several syntheses have been developed in recent years to obtain mixed-valence transition metal oxides. Among the most common methods for obtaining (Mn-Co-O) are the sol-gel [31], combustion [32], solvothermal [33], solid-state [34], co-precipitation [35], spray pyrolysis [36], and hydrothermal [37] methods. These processes directly influence the morphology and/or structure of the materials, especially the sol-gel method, which allows crystalline materials to be obtained [38,39].

However, another method that has been attracting the attention of many researchers is that named proteic sol-gel synthesis, which is defined as a modification of the traditional sol-gel method, and allows ceramic materials to be obtained at the nanometer scale [40]. This method involves the following steps: preparation of a composite solution, formation of an amorphous network via polymerization reactions, followed by hydrolysis, gel formation, removal of organic residues and water, and finally calcination [41,42]. In this context, the proteic sol-gel method has several advantages over the traditional method, such as simplicity, low cost, higher speed, and generation of less waste to the environment [43,44], since it employs organic precursors, which are called polymerizing agents, having the function of replacing citric acid and ethylene glycol as driving agents of the reaction. Furthermore, these agents have hydroxyl and carboxyl groups that promote the chelation of metal ions during the synthesis process [45]. Some examples of organic precursors are flavorless gelatin [46], coconut water [47], and Agar-Agar [48].

Agar-Agar is a biopolymer [49], hydrocolloid [50] and polysaccharide source [51], extracted from red algae of the class Rhodophyceae [52], which is composed of two main parts: agarose, which is responsible for the gelling ability, and agaropectin, which is the polymeric part resulting from the existence of various substituent groups, such as sulfates and methyl ethers among others [53]. Due to its gelling properties, biocompatibility, biodegradability, and non-toxicity [54], Agar-Agar is used in the food, leather, cosmetic, beverage, and pharmaceutical industries [55].

The present work aims to investigate the structural, optical, and magnetic properties through the Co/Mn ratios in the structure, as well as the electrochemical properties of $Mn_xCo_{3-x}O_4$ -type mixed-valence transition metal oxide powders synthesized by the proteic sol-gel method using Agar-Agar as a polymerizing agent.

2. Experimental Section

2.1. Materials

Cobalt nitrate ($Co(NO_3)_2 \cdot 6H_2O$, (Sigma-Aldrich 99%, Saint-Louis, MO, USA), manganese nitrate ($Mn(NO_3)_2 \cdot 4H_2O$, Vetec 99%, Saint-Louis, MO, USA), and Agar-Agar

(Gelialgas-Agargel, João Pessoa, Brazil) were used in the present study. Nickel foam (Ni 99.8%, porosity >95%) was purchased from QiJing Ltd., Ninghai, China.

2.2. Synthesis of the Proteic Sol-Gel Using Agar-Agar

The scheme of $Mn_xCo_{3-x}O_4$ ($0 \leq x \leq 1$) preparation is shown in Figure 1. The mixed oxides were synthesized using $Co(NO_3)_2 \cdot 6H_2O$ and $Mn(NO_3)_2 \cdot 4H_2O$, while Agar-Agar was used as the polymerizing agent. First, 2.0 g of Agar-Agar was dispersed in 50 mL of distilled water at 60 °C, then the proper amounts in mols of the metal salts were added as follows for samples with $x = 0.0$ (cobalt nitrate: 0.0249 mol), $x = 0.2$ (cobalt nitrate: 0.0233 mol and manganese nitrate: 1.6673 mmol), $x = 0.4$ (cobalt nitrate: 0.0217 mol and manganese nitrate: 3.3437 mmol), $x = 0.6$ (cobalt nitrate: 0.0201 mol and manganese nitrate: 5.0337 mmol), $x = 0.8$ (cobalt nitrate: 0.0185 mol and manganese nitrate: 6.7332 mmol), and $x = 1.0$ (cobalt nitrate: 0.0169 mol and manganese nitrate: 8.4459 mmol), and the resulting solution was kept under stirring at 90 °C until the formation of a gel. The resulting gel was kept at 350 °C for 2 h. Hence, the obtained powders were ground and calcined in air at 900 °C. The samples $Mn_xCo_{3-x}O_4$ were labeled as: for $x = 0.0$ (Co_3O_4), $x = 0.2$ ($Mn_{0.2}Co_{2.8}O_4$), $x = 0.4$ ($Mn_{0.4}Co_{2.6}O_4$), $x = 0.6$ ($Mn_{0.6}Co_{2.4}O_4$), $x = 0.8$ ($Mn_{0.8}Co_{2.2}O_4$) and $x = 1.0$ ($MnCo_2O_4$).

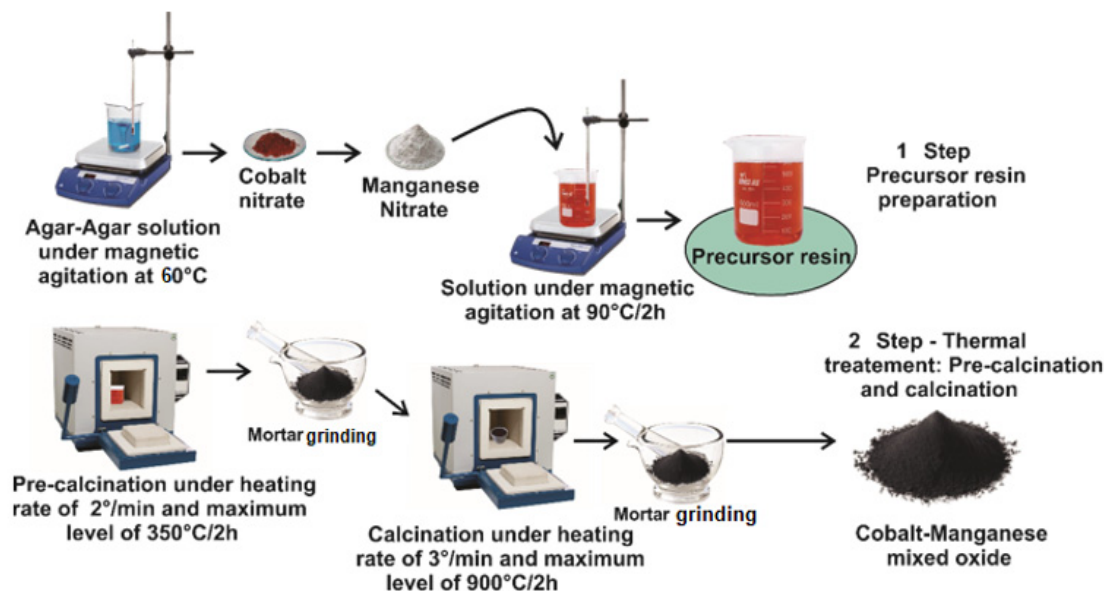


Figure 1. Procedure for the synthesis of samples $Mn_xCo_{3-x}O_4$ ($0 \leq x \leq 1$).

2.3. Structural and Morphological Characterization

X-ray powder diffraction patterns (XRD) were obtained by a Shimadzu XRD-7000 diffractometer using $K\alpha(Cu) = 1.5481 \text{ \AA}$ radiation. The 2θ range was investigated from 10° to 80° with a step size of 0.02° and acquisition time of 1 s. The crystallite size, lattice parameters, and atomic positions were determined by Rietveld refinement using the software Materials Analysis Using Diffraction (TOPAS). FT-IR spectra were performed by a Shimadzu IRPrestige21 spectrophotometer between 500 and 4000 cm^{-1} , using KBr pellets. The ultraviolet–visible spectra (UV–Vis) were obtained in the UV-2600i spectrophotometer from Shimadzu. SEM images were obtained by a field-emission scanning electron microscope (FESEM, Carl Zeiss, Supra 35-VP Model) equipped with a Bruker EDS detector (XFlash 410-M). Surface chemical states were studied by X-ray photoelectron spectroscopy (XPS) using a SPECS Phoibos 150 spectrometer with a high-intensity monochromatic Al-K α X-ray source (1486.6 eV). Samples were dispersed in acetone and deposited on silicon by drop-coating. Adventitious carbon C 1s with binding energy at 284.8 eV was used as reference energy. CasaXPS software was used for spectra deconvolution, thus obtaining the height, area, and position of the analyzed peaks. All the symmetric peaks were fitted

using Gaussian and Lorentzian functions. Magnetic measurements were obtained using a vibrating sample magnetometer (VSM) from Lakeshore, model 7400, at room temperature, with a maximum magnetic field applied up to +15.0 KOe.

2.4. Electrochemical Characterization

All electrochemical studies were performed in an alkaline aqueous solution (KOH, 1 M pH = 13.6) at room temperature by a PGSTAT204 with FRA32M module (Metrohm Autolab) using a three-electrode setup with a platinum plate and Hg/HgO as counter and reference electrodes, respectively. The samples $\text{Mn}_x\text{Co}_{3-x}\text{O}_4$ ($0 \leq X \leq 1$) were used for the fabrication of the working electrodes. Catalytic inks were prepared by mixing 5 mg of each catalyst with 50 μL of Nafion solution (5 wt%) and dispersing the mixture in 500 μL of isopropyl alcohol. Then, inks were drop-casted onto Ni foams ($1 \times 1 \text{ cm}$) on clean substrates and dried at room temperature for 5 h to prepare the working electrodes. Linear sweep voltammetry (LSV) was performed at 5 mV s^{-1} . Electrochemical impedance spectroscopy (EIS) was carried out using dc potentials (1.4 V vs. RHE) in the frequency range of 0.1 Hz–10 kHz and voltage amplitude of 10 mV. All measured potentials (with iR correction) were converted to the reversible hydrogen electrode (RHE) using the Nernst equation ($E_{\text{RHE}} = E_{\text{Hg}/\text{HgO}} + 0.059 \times \text{pH} + 0.098$). Overpotential (η) values were calculated by the equation $\eta = E_{\text{RHE}} - 1.23 \text{ V}$. The stability tests were conducted by chronopotentiometry analysis using multi-steps of $10\text{--}20 \text{ mA cm}^{-2}$. Figure 2 shows the complete characterization process.

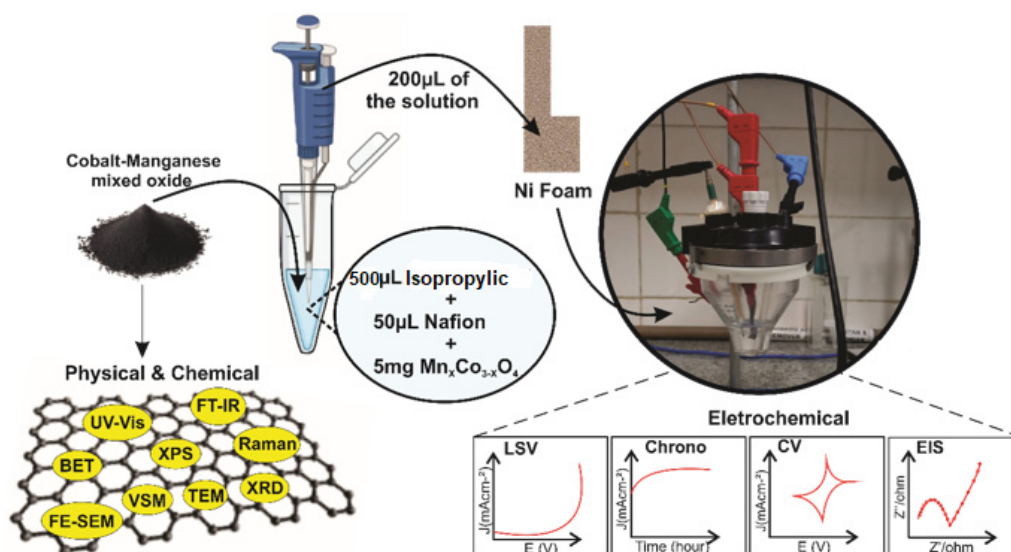


Figure 2. Physical, chemical, and electrochemical characterization of $\text{Mn}_x\text{Co}_{3-x}\text{O}_4$ ($0 \leq X \leq 1$).

3. Results

3.1. X-ray Diffraction (XRD)

The refined X-ray diffraction patterns of the $\text{Mn}_x\text{Co}_{3-x}\text{O}_4$ ($0 \leq X \leq 1$) are shown in Figure 3a. As noted, all peaks are characteristic of the cubic phases of Co_3O_4 (structure of Spinel# MgAl_2O_4 type, with lattice parameter $a = b = 8.072(3) \text{ \AA}$, ICSD n° 36256, space group Fd-3mS (227)) [56] and MnCo_2O_4 (structure of Spinel# MgAl_2O_4 type, with lattice parameter $a = b = 8.28(2) \text{ \AA}$, ICSD n° 18544, space group Fd-3mZ (227)) [57]. No secondary phases corresponding to impurities were detected. The ICSD n° 36,256 was used to fit the $\text{Mn}_x\text{Co}_{3-x}\text{O}_4$ samples ($X < 1$), while the 18,544 ICSD file was applied to refine the sample with composition $X = 1$. The observed patterns are similar to those reported previously for pure and doped cobaltites [16,20,58]. All crystallographic parameters, including crystallite size and lattice parameter, as well as the agreement indices (R_{wp} , R_{exp} e χ^2) for samples of $\text{Mn}_x\text{Co}_{3-x}\text{O}_4$ ($0 \leq X \leq 1$) are gathered in Table 1.

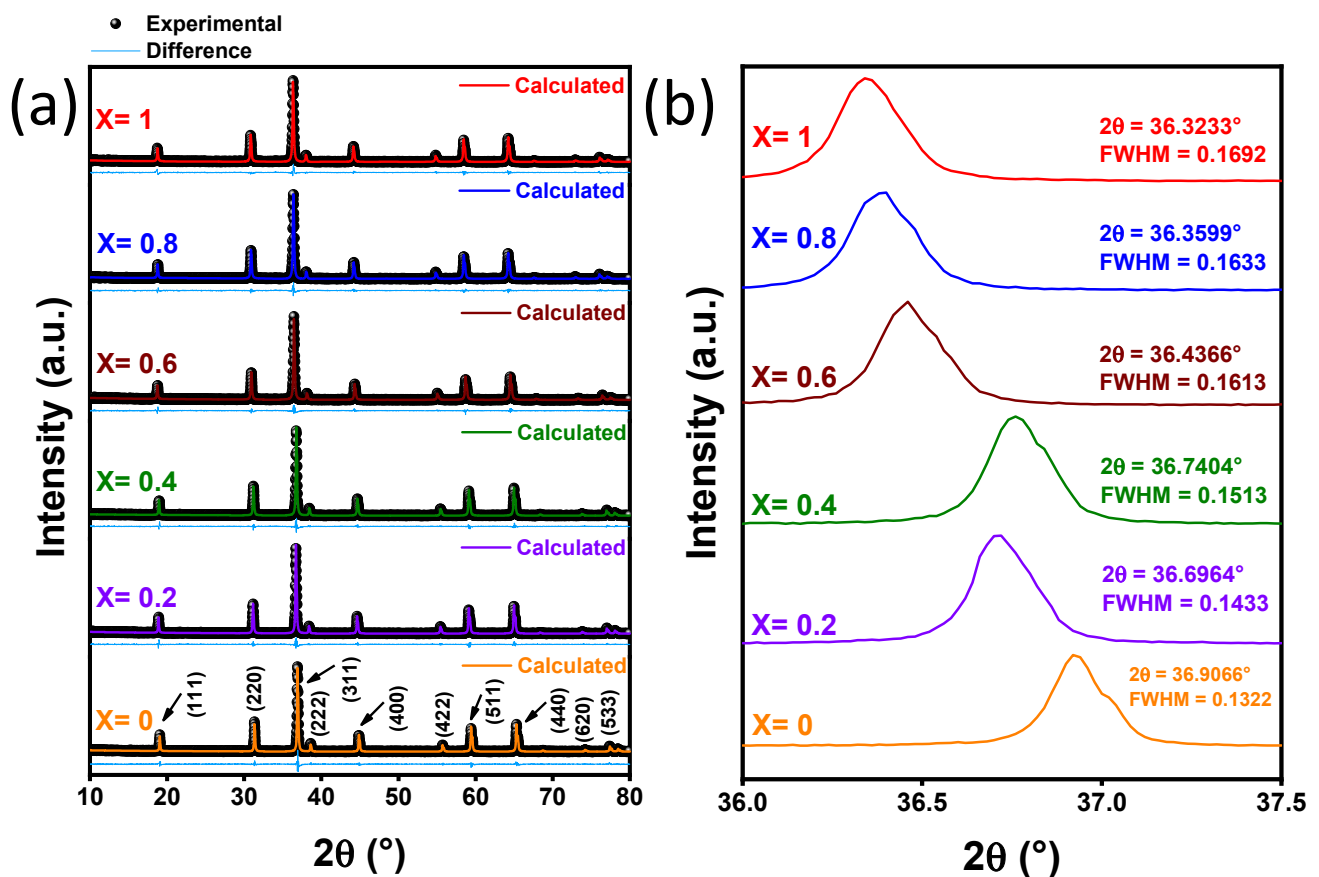


Figure 3. (a) XRD patterns of $\text{Mn}_x\text{Co}_{3-x}\text{O}_4$ ($0 \leq x \leq 1$) samples (b) Peaks (311) for each sample and their positions and FWHM. Blue lines below the diffractograms are the difference between the calculated and experimental data.

Table 1. Crystallographic parameters, including crystallite size, lattice parameter, and agreement indices (R_{wp} , R_{exp} e χ^2) for samples of $\text{Mn}_x\text{Co}_{3-x}\text{O}_4$ ($0 \leq x \leq 1$).

Samples	Co_3O_4 —ICSD 36256		MnCo_2O_4 —ICSD 18544		Agreement Factors		
	D_{XRD} (nm)	a (Å)	D_{XRD} (nm)	a (Å)	R_{wp} (%)	R_{exp} (%)	χ^2
Co_3O_4 —ICSD 36256	—	8.072(3)	—	—	—	—	—
MnCo_2O_4 —ICSD 18544	—	—	—	8.28(2)	—	—	—
X = 0	90.6 [100%]	8.0757(1)	—	—	7.16	6.92	1.04
X = 0.2	82.5 [100%]	8.0759(8)	—	—	7.95	6.59	1.21
X = 0.4	80 [100%]	8.0754(1)	—	—	7.97	6.60	1.21
X = 0.6	71 [100%]	8.1183(7)	—	—	8.14	6.67	1.22
X = 0.8	68.8 [100%]	8.1675(8)	—	—	8.01	6.66	1.20
X = 1	—	—	66 [100%]	8.2381(6)	8.69	6.70	1.30

Figure 3b shows the magnification of the most intense diffraction peak (311), located between 36° and 37.5° . As shown, increasing Mn content shifts the (311) peak to lower angles, indicating a continuous increase in the lattice parameter from 8.0757(1) for $x = 0$, 8.0759(8) for $x = 0.2$, 8.1183(7) for $x = 0.6$, 8.1675(8) for $x = 0.8$ to 8.2381(6) for $x = 1$. The total width at half maximum intensity (FWHM) also increases gradually with the increase in Mn (0.1322 for $x = 0$, 0.1433 for $x = 0.2$, 0.1513 for $x = 0.4$, 0.1613 for $x = 0.6$, 0.1633 for $x = 0.8$ and 0.1692 for $x = 1$), signaling a progressive reduction in crystallite size and increase in strain (90.6 nm for $x = 0$, 82.5 nm for $x = 0.2$, 80 nm for $x = 0.4$, 71 nm for $x = 0.6$, 68.8 nm for $x = 0.8$, 66 nm for $x = 1$, with the only exception of the sample corresponding to $X = 0.4$ for which the 2θ angle is slightly higher than the one displayed by the sample with

$X = 0.2$). The largest variations of FWHM occur in the $0 \leq X \leq 0.6$ range. The Mn^{+2} has a radius of 0.80 Å and it is larger than the radii of Co^{+3} (0.63 Å) and Co^{+2} (0.65 Å); thus, it causes distortion and strain in the Co_3O_4 lattice, resulting in a decrease in crystallite size. In addition, other manganese oxidation states may be present in the samples such as Mn^{+3} and Mn^{+4} . Mn^{+3} ($3d^4$) is responsible for the Jahn–Teller phenomenon, which also develops a distortion in the lattice and an intrinsic strain that leads to a decrease in the crystallite size [20,59–61]. The trends of lattice parameter and crystallite size are in agreement with previous reports [16,20]. The maximum values of the agreement factors R_{wp} and R_{exp} from the Rietveld analyses are 8.14% and 6.92%, respectively. The low values of fitting quality ($\chi^2 \leq 1.30$) indicate excellent agreement between the data and the refined models.

3.2. Field-Emission Scanning Electron Microscopy (FESEM)

The FESEM images of the $\text{Mn}_X\text{Co}_{3-X}\text{O}_4$ nanoparticles ($0 \leq X \leq 1$) are shown in Figure 4. A non-uniform morphology was observed, specifically polyhedral-shaped particles, and a few smaller spherical-like particles, mostly agglomerated [38]. Another observation is that as the amount of Mn increases, the morphology of particles tends to be octahedral like. The average particle size distribution was 208 nm for $X = 0.0$, 162 nm for $X = 0.2$, 145 nm for $X = 0.4$, 142 nm for $X = 0.6$, 140 nm for $X = 0.8$, and 133 nm for $X = 1.0$. From the size distribution histograms, it is evident the shift of main sizes to smaller values as the Mn content increased.

3.3. Transmission Electron Microscopy (TEM)

Additional morphological characterization was carried out by the TEM technique. Typical images of the nanoparticles are presented in Figure 5. They show particles with non-uniform morphologies of different sizes. These pictures agree well with the images acquired by FESEM (Figure 4). Figure 5b,e,h,k,n,q shows high-resolution TEM images (5 nm scale) of particles larger than 10 nm in size, with fringes related to atomic planes with spacings of 0.24, 0.296, 0.282, 0.252, 0.303, and 0.486 nm that may be due to the planes (311), (220), (220), (311), (220) and (111) for samples $X = 0.0$, $X = 0.2$, $X = 0.4$, $X = 0.6$, $X = 0.8$ and $X = 1.0$, respectively. Furthermore, it appears that the particles are coated with a carbon layer with a thickness smaller than 5 nm. Figure 5c,f,i,l,o,r shows the small-area electron diffraction (SAED) patterns of the samples. They exhibit diffraction rings originating from crystal planes (111), (220), (311), (400), (422), (333), and (440). The planes are listed beginning from the smallest ring.

3.4. Fourier-Transform Infrared (FT-IR) Spectroscopy

The FT-IR technique shows the vibrational fingerprint of the sample, with absorption peaks that correspond to the frequencies of vibrations of the bonds among the atoms that make up the material [62]. Figure 6 shows the spectra of the $\text{Mn}_X\text{Co}_{3-X}\text{O}_4$ samples ($0 \leq X \leq 1$) in the range from 400 to 4000 cm^{-1} , where two bands with the highest intensities are located at 552–570 and 643–663 cm^{-1} , which are related to the stretching vibrations of the metal–oxygen bond, which confirms the formation of the pure Co_3O_4 phase [63]. The ν_1 band at 552–570 cm^{-1} is characteristic of the vibration of Co^{3+} at the octahedral site, and the ν_2 band at 643–663 cm^{-1} is related to the vibration of Co^{2+} at the tetrahedral site, confirming the formation of the spinel-like oxide [64], in agreement with the XRD study. The low-intensity band that appears at 1100 cm^{-1} is due to C–O stretching vibrations. The band at 1383 cm^{-1} is attributed to the symmetric deformations of C–N and CH_2 groups, originating from the residues of nitrate ions and agar-agar [65–67]. The band at 1635 cm^{-1} was attributed to the angular deformation of the adsorbed water molecules [68]. The broad absorption band in the region of about 3440 cm^{-1} is due to OH stretching of the water molecules adsorbed from the moisture during the storage process [69]. Furthermore, it is observed that the bands at 554–643 cm^{-1} for sample $X = 0.8$ and the bands at 552–643 cm^{-1} for sample $X = 1.0$ are similar, which may be related to the oxidation states of manganese (Mn^{+2} , Mn^{+3} , and Mn^{+4}) or to the vibrational intensity between the manganese and oxygen

bond. In general, the frequency of the peaks of the absorption bands at (552–570) and (643–663) cm^{-1} (Table 2) decreases with the replacement of cobalt with manganese ions, i.e., they shift to the right as the amount of manganese increases, and this is related to the increase in the metal–oxygen distance, as indicated by the increase in the lattice parameter of the unit cells (Table 1), since Mn ions are larger than Co ions [21].

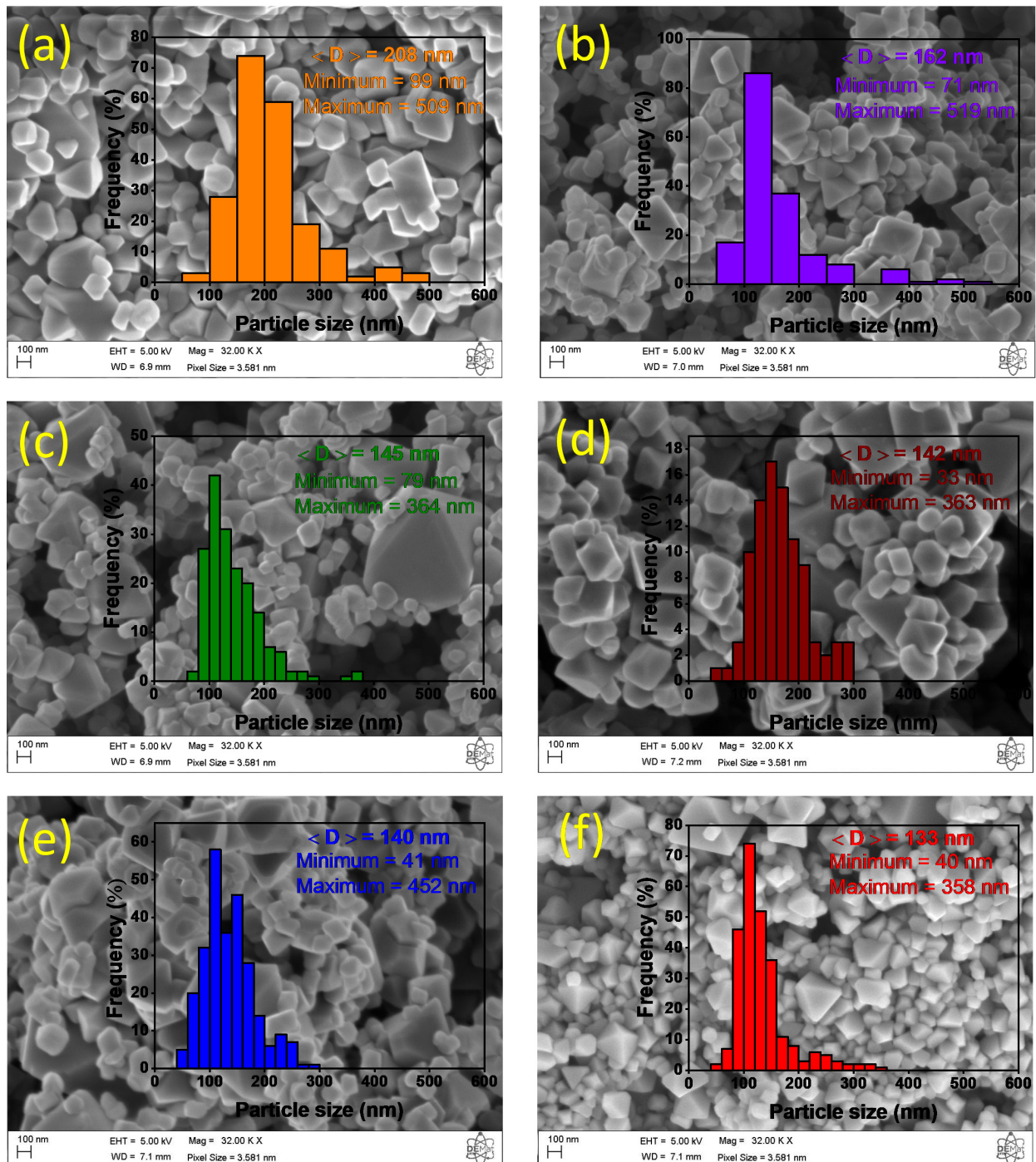


Figure 4. FESEM images and particle size distribution of $\text{Mn}_x\text{Co}_{3-x}\text{O}_4$ ($0 \leq x \leq 1$) samples (a): $X = 0.0$, (b) $X = 0.2$, (c) $X = 0.4$, (d) $X = 0.6$, (e) $X = 0.8$, and (f) $X = 1.0$.

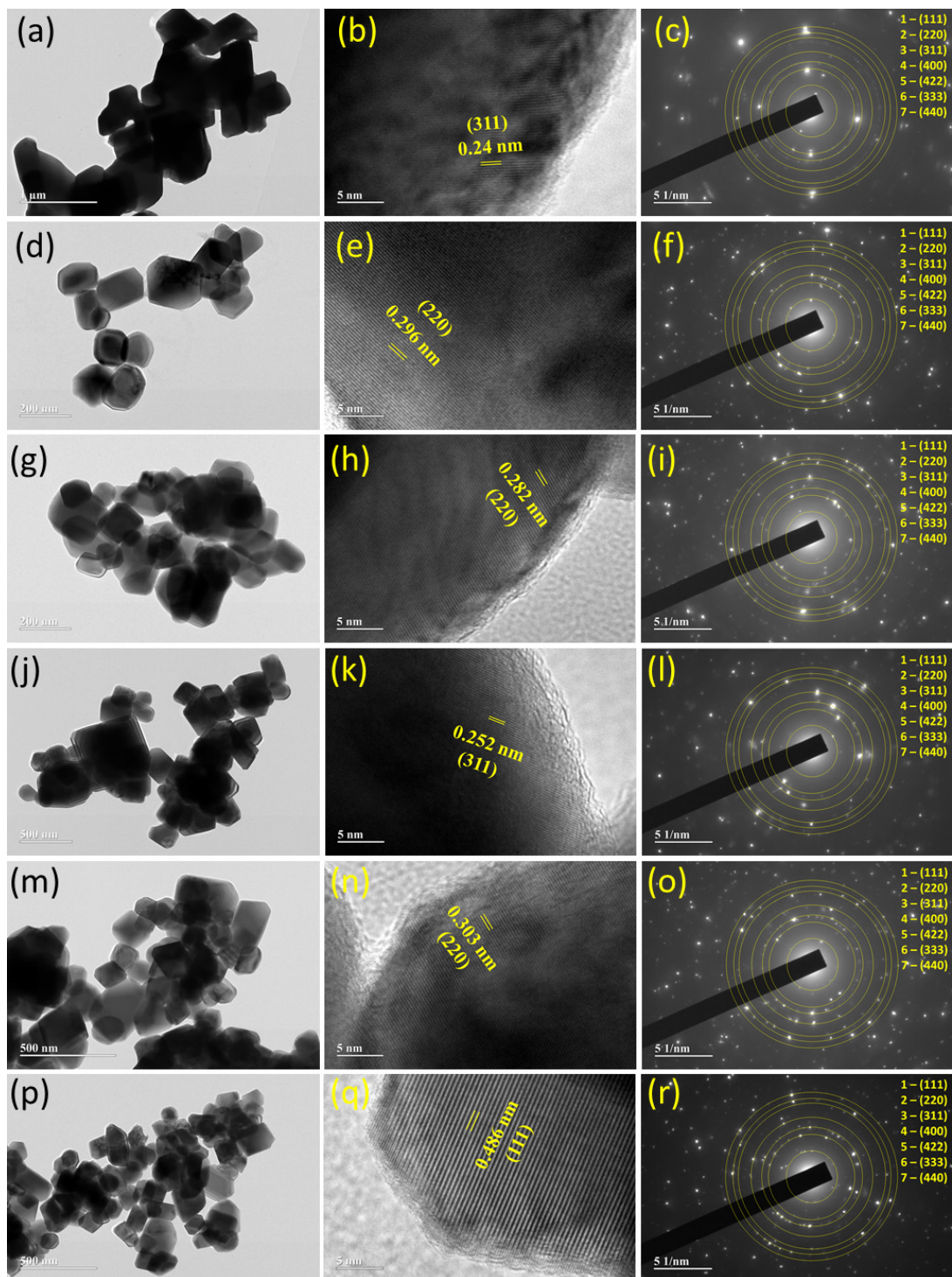


Figure 5. TEM images and selected area electron diffraction (SAED) of $\text{Mn}_X\text{Co}_{3-X}\text{O}_4$ ($0 \leq X \leq 1$) samples: (a–c) $X = 0.0$, (d–f) $X = 0.2$, (g–i) $X = 0.4$, (j–l) $X = 0.6$, (m–o) $X = 0.8$, and (p–r) $X = 1.0$.

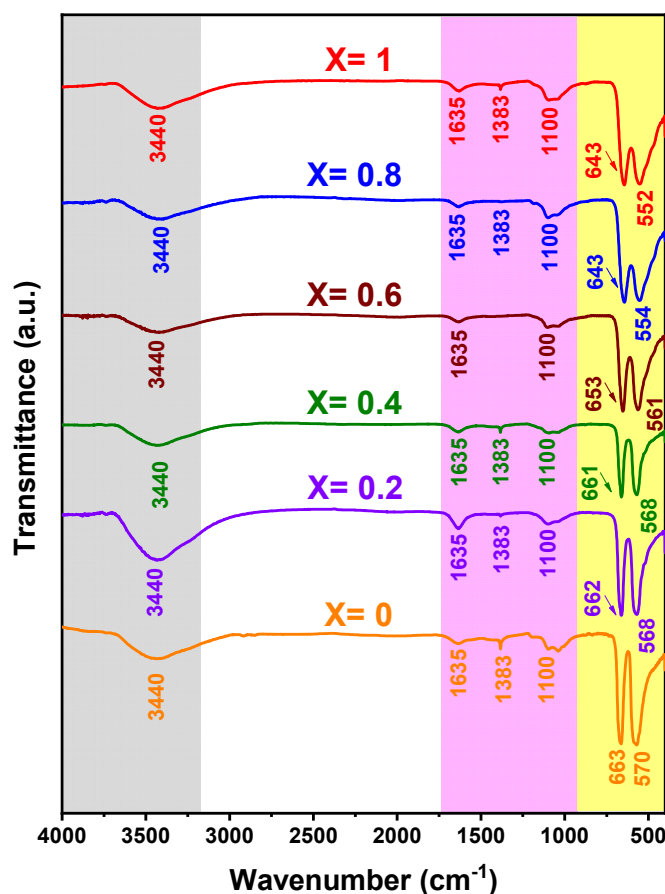


Figure 6. FT-IR spectra for all $Mn_XCo_{3-X}O_4$ ($0 \leq X \leq 1$) samples.

Table 2. Assignment of the FT-IR band frequencies observed for $Mn_XCo_{3-X}O_4$ ($0 \leq X \leq 1$) samples and their comparison with the literature.

Observed Frequencies (cm^{-1})						Reference	Mode Assignment
(X = 0.0)	(X = 0.2)	(X = 0.4)	(X = 0.6)	(X = 0.8)	(X = 1.0)		
3440	3440	3440	3440	3440	3440	[68–72]	O-H stretching vibration
1635	1635	1635	1635	1635	1635	[65,68,71,73,74]	Angular deformation of adsorbed water molecules
1383	1383	1383	1383	1383	1383	[65–67]	Deformations of C-N and CH ₂ groups
1100	1100	1100	1100	1100	1100	[62,68,74]	C-O stretching vibrations
663	662	661	653	643	643	[65,68,70,71,75]	Stretching vibrations of Mn–O
570	568	568	561	554	552	[21,63,64,72,73]	Stretching vibrations of Co–O

3.5. Ultraviolet–Visible Spectroscopy (UV–Vis)

The electronic properties of $Mn_XCo_{3-X}O_4$ samples, as illustrated in Figure 7, were investigated by UV–Vis spectroscopy in the wavelength range from 300 to 1400 nm. The absorptions at 528 and 792 nm for the sample $X = 0$ correspond to the ligand–metal O(-II) \rightarrow Co(III) and O(-II) \rightarrow Co(II) electron transfer, respectively [76–78]. The variation of absorption in the range from 1033 to 1110 nm shows that when the amount of manganese increases, the absorption peak wavelength increases, and this is related to the higher O₂/O₁ ratios according to the XPS results, and it will affect the overpotential in the oxygen evolution reaction for the $MnCo_2O_4$ ($X = 1.0$) sample, which would mean a better catalytic activity for the oxidation reactions.

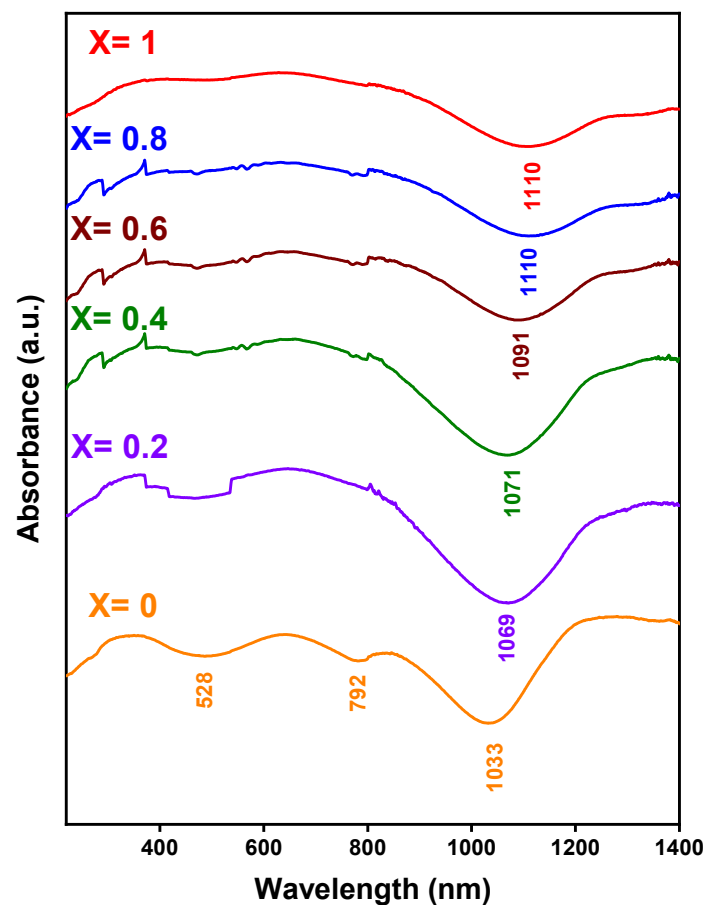


Figure 7. UV-Vis Absorbance spectra of $Mn_xCo_{3-x}O_4$ ($0 \leq X \leq 1$) samples.

3.6. Raman Spectroscopy

Figure 8 shows the Raman spectra of the $Mn_xCo_{3-x}O_4$ samples in the range from 100 to 1000 cm^{-1} . The observed bands in the intervals 193–688 cm^{-1} for $x = 0.0$, 186–682 cm^{-1} for $x = 0.2$, 186–675 cm^{-1} for $x = 0.4$, 185–667 cm^{-1} for $x = 0.6$, 183–661 cm^{-1} for $x = 0.8$, and 182–660 cm^{-1} for $x = 1.0$ correspond to the active Raman modes $A_{1g}+E_g+3F_{2g}$ (Table 3), confirming the formation of the pure phase of mixed-valence oxides of spinel-like structure [79–83]. The most intense band at 688–660 cm^{-1} is assigned to the octahedral site MO_6 related to the A_{1g} mode of the O_{7h} spectroscopic symmetry, which corresponds to the stretching vibrational modes of these oxides M–O, where $M = \{Co, Mn\}$, thus substantiating the formation of $MnCo_2O_4$. The Raman bands with medium intensity in the intervals 468–488 cm^{-1} and 508–518 cm^{-1} are assigned to E_g and F_{2g} , respectively; meanwhile, the Raman bands with lower intensities in the interval 603–617 cm^{-1} are caused by the F_{2g} mode. Moreover, the Raman bands with very low intensity at 182–193 cm^{-1} are attributed to the F_{2g} mode related to the tetrahedral sites of CoO_4 [82–84]. In general, when comparing the positions of the peaks, it is observed that as the amount of manganese increases, the peaks shift to the left, analogously to what was noticed in the FT-IR spectra. This change may be due to the greater ionic radius of Mn^{2+} , in comparison to that of Co^{2+}/Co^{3+} [85–87], which when entering the structure of Co_3O_4 , generates a large distortion in the crystalline structure and increases the distance between the metal and the oxygen, and consequently a weakening of bonds occurs. Another reason would be due to vibrations in the structure, where the Co^{2+} and Co^{3+} cations are located in tetrahedral and octahedral sites in the cubic crystal structure [88].

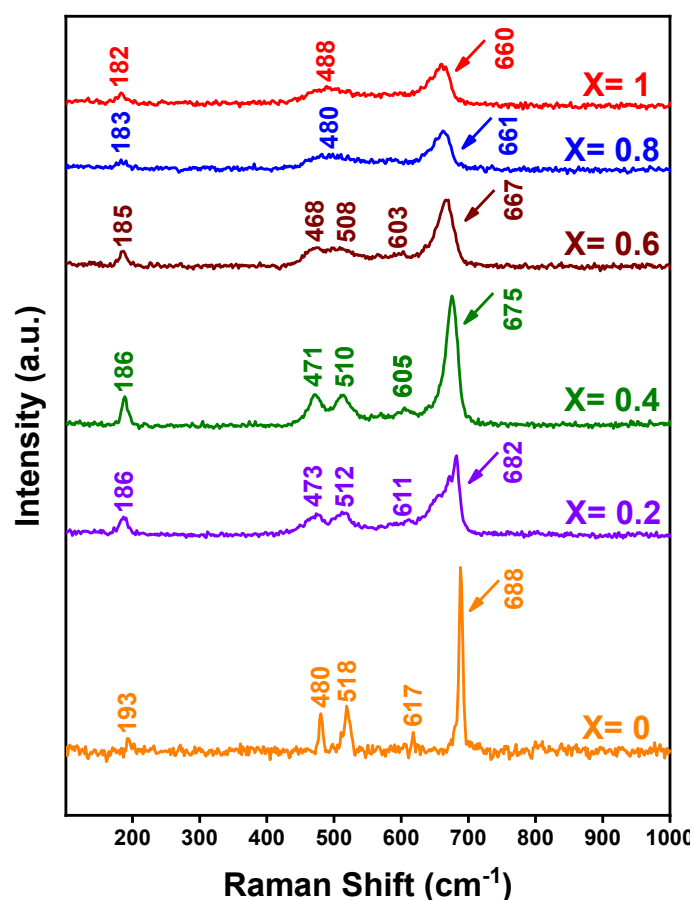


Figure 8. Raman spectra for all $Mn_XCo_{3-X}O_4$ ($0 \leq X \leq 1$) samples.

Table 3. Raman active band positions for $Mn_XCo_{3-X}O_4$ ($0 \leq X \leq 1$) samples and their comparison with the literature.

$Mn_XCo_{3-X}O_4$ ($0 \leq X \leq 1$)	Raman Band Position (cm^{-1})					Reference
	F2g	Eg	F2g	F2g	A1g	
(X = 0.0)	193	480	518	617	688	[82–84]
(X = 0.2)	186	473	512	611	682	[20,88]
(X = 0.4)	186	471	510	605	675	[81,82]
(X = 0.6)	185	468	508	603	667	[20,83]
(X = 0.8)	183	480	-	-	661	[82,89]
(X = 1.0)	182	488	-	-	660	[79,80]

3.7. X-ray Photoelectron Spectroscopy (XPS)

The surface oxidation states of the samples were analyzed by XPS. Figure 9 shows the high-resolution Co 2p, Mn 2p, and O 1s spectra obtained from the analysis. All data were corrected for the carbon peak position. In the case of the Co 2p spectra (Figure 9a), four peaks were deconvoluted, at lower binding energies, corresponding to Co^{3+} and Co^{2+} , as well as two satellite peaks at higher binding energies. The binding energies obtained for Co^{3+} were found to fall in the 779.64–780.19 eV range, while for Co^{2+} , in the 781.19–781.85 eV range, in agreement with previous work [90]. We also found a Co^{2+}/Co^{3+} ratio varying from 0.31 to 0.40 among the samples, for which the sample X = 0.8 was found to have the lowest value of $Co^{2+}/Co^{3+} = 0.31$. Higher oxidation states can induce more bonded oxygen species, which may have a positive impact on oxidation reactions.

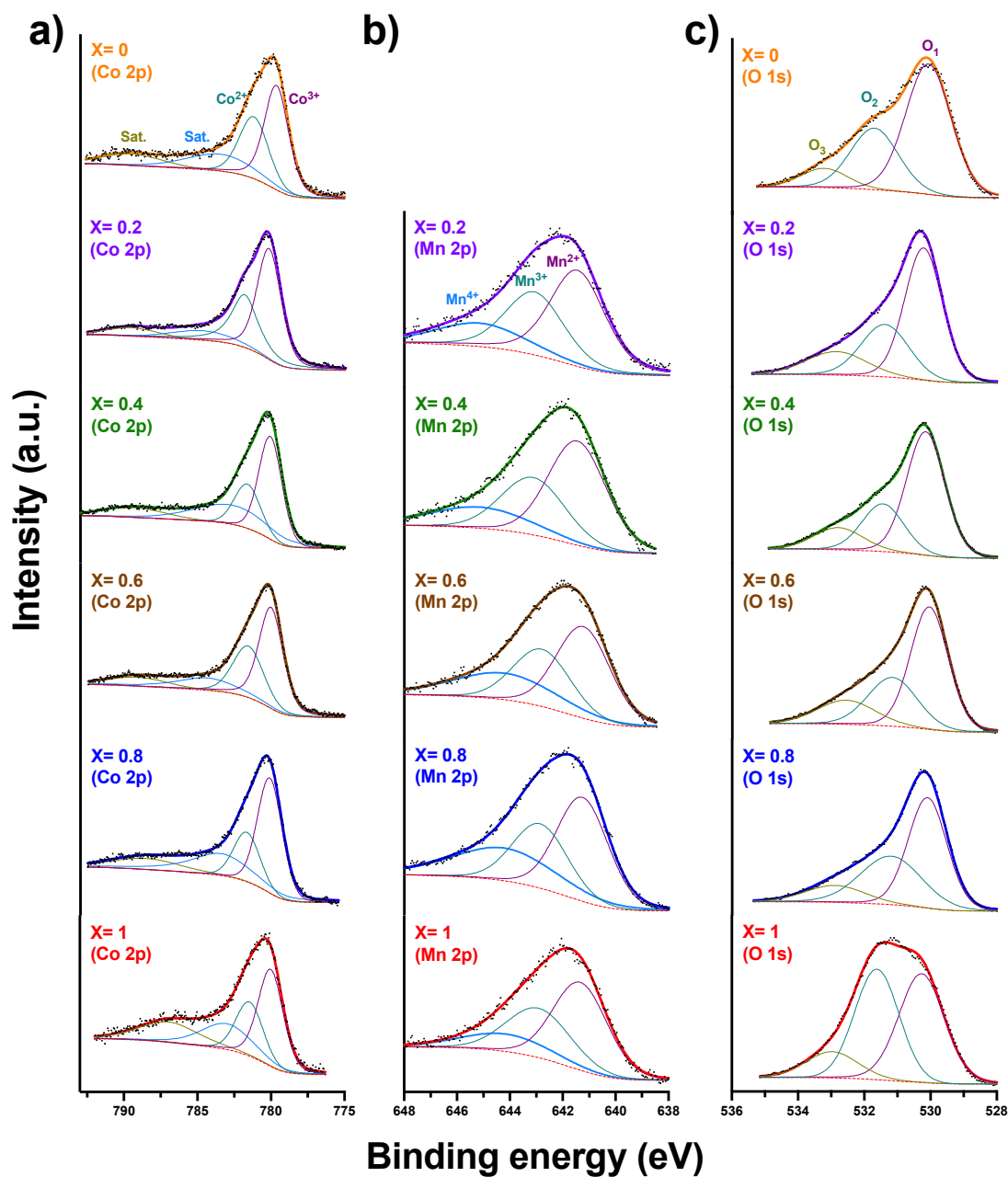


Figure 9. High-resolution XPS spectra of $\text{Mn}_x\text{Co}_{3-x}\text{O}_4$ ($0 \leq x \leq 1$) for (a) Co 2p, (b) Mn 2p and (c) O 1s.

Conversely, in the case of the Mn 2p spectra (Figure 9b), the data were deconvoluted into three peaks, which were ascribed to Mn^{4+} (ranging from 644.154 eV to 645.146 eV), Mn^{3+} (ranging from 642.790 eV to 643.125 eV), and Mn^{2+} (641.223 eV to 641.459 eV), in agreement with previous reports [90,91]. The lowest oxidation state species, Mn^{2+} , was found to represent the largest fraction of the total species present at the surface, with a relative value varying from 0.42 to 0.51 among the samples. Conversely, the presence of Mn^{4+} and Mn^{3+} oxidation states is related to the relatively high calcination temperature used in this work, i.e., 900 °C, as found in previous literature [92]. In this respect, we also noted a higher $\text{Mn}^{3+}/\text{Mn}^{4+}$ ratio for the tested samples, which correlates well with the previously discussed Jahn–Teller phenomenon, with a concurrent distortion of the crystal lattice.

Finally, the O 1s high-resolution spectra (Figure 9c) display three deconvoluted peaks: O_1 (529.94–530.27 eV), O_2 (531.16–531.72 eV), and O_3 (532.55–533.19 eV). Based on the char-

characteristic binding energies determined for these peaks, they are likely related to surface lattice oxygen (O_{lat}, O^{2-}), adsorbed oxygen species ($O_{\text{ads}}, O^{2-}, O_2^{2-}$, and O^-), and adsorbed water species ($O_{\text{H}_2\text{O}}$), in agreement with earlier reports on similar compounds [91,93]. From the analysis of the O 1s high-resolution spectra (Table 4), we determined higher O_2/O_1 ratios with increasing Mn content, with a maximum value obtained for the $X = 1.0$ sample. This suggests that the compounds with the highest Mn content possess increased catalytic activity, as a likely result of increased oxygen-ion vacancies in these samples.

Table 4. Gaussian-fitted peaks for O 1s XPS spectra for $\text{Mn}_X\text{Co}_{3-X}\text{O}_4$ ($0 \leq X \leq 1$) samples.

Sample	X = 0	X = 0.2	X = 0.4	X = 0.6	X = 0.8	X = 1
Peak (eV)	531.717	531.386	531.448	531.158	531.195	531.618
O_2 area (nm)	9859.487	12887.39	13100.65	13363.590	15330.310	19922.580
O_2/O_1	0.495	0.498	0.502	0.517	0.693	0.940

3.8. Vibrating Sample Magnetometer (VSM)

Magnetization measurements were done to study the magnetic behavior of samples at room temperature and to determine the cation magnetic moment in an approximate manner. For all samples, the isothermal magnetization at $T = 300$ K showed a linear behavior with the magnetic field, and their magnetization at a given field increased with the Mn concentration, as shown in Figure 10.

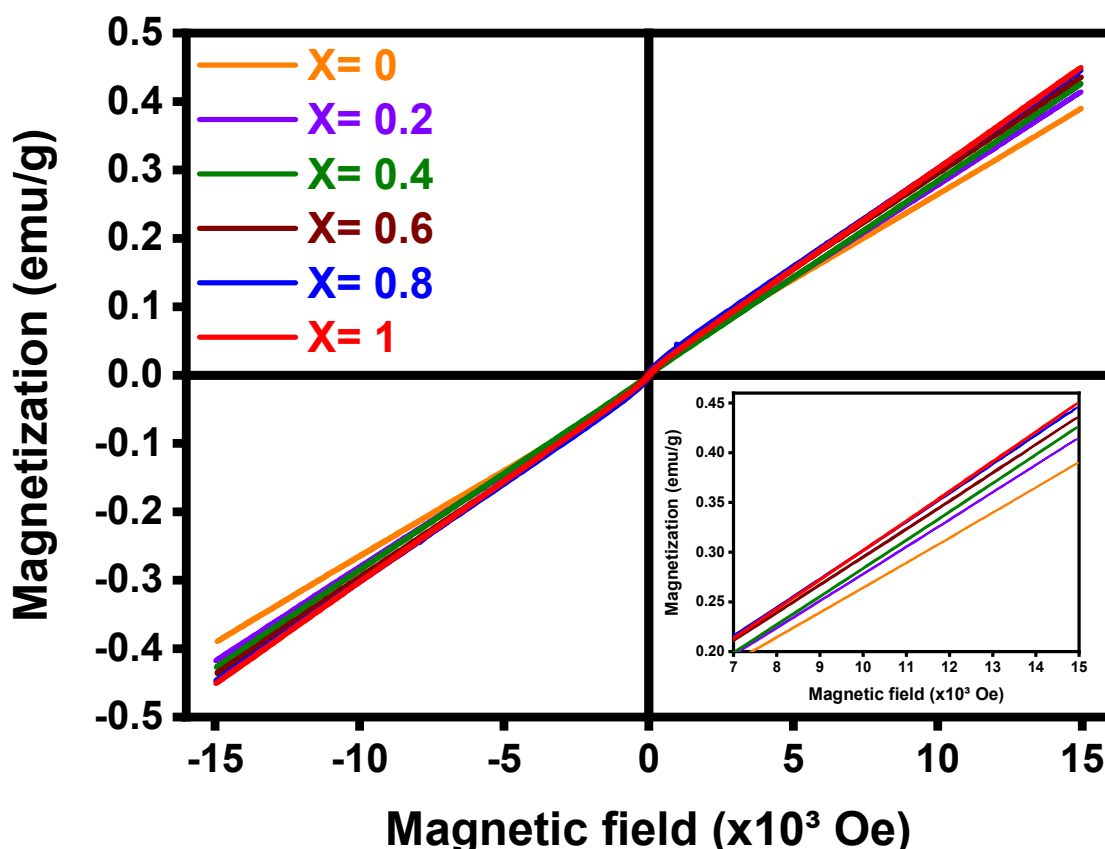


Figure 10. Magnetization curve of $\text{Mn}_X\text{Co}_{3-X}\text{O}_4$ ($0 \leq X \leq 1$).

This trend was observed for all samples and it is typical of paramagnetic samples as shown in Figure 10. From the classical theory of paramagnetism we know that the relationship between the magnetization (M) and magnetic field (H) is given by the Langevin function $L(a) = M/M_0 = \coth(a) - 1/a$, where M and M_0 are the mass magnetizations per total amount of Mn and Co (without oxygen), $a = \mu H/K_B T$, μ is the average magnetic moment

per cation, K_B is the Boltzmann constant ($1.3807 \times 10^{-16} \text{ cm}^2\text{gK/s}^2$), and $T = 300 \text{ K}$. It is known that $L(a)$ tends to $a/3$ when a is less than about 0.5 [94]. In the present case, if $\mu \sim 4.51 \times 10^{-20} \text{ Erg/Oe}$ (theoretical magnetic moment for Mn^{3+} and Co^{3+}) and $H = 15 \times 10^3 \text{ Oe}$, then, one can get $a = 0.01633$, which is smaller than 0.5. Thus, $L(a) = M/M_0 \approx a/3$ and, therefore, $M = [M_0\mu/(3K_B T)]H$. In a paramagnetic system $M_0 = N\mu/A$, where N is the Avogadro's number and $A = (x*54.938 + (3-x)*58.933)/3$ is the average atomic mass provided by Mn and Co in $\text{Mn}_x\text{Co}_{3-x}\text{O}_4$ (where $X = \{0.0, 0.2, 0.4, 0.6, 0.8, 1.0\}$). Thus, the DC susceptibility is $\chi = M/H = N\mu^2/(3AK_B T)$ [94]. One can study the M-H data by fitting the curve to a linear equation and comparing the slope to $N\mu^2/(3AK_B T)$. Then, to obtain μ in Bohr magnetons (μ_B), one has to calculate $\mu/0.9274 \times 10^{-20}$. The results provided an effective magnetic moment per cation of 2.204, 2.294, 2.342, 2.344, 2.348, 2.378 μ_B for the samples prepared with $x = 0.0, 0.2, 0.4, 0.6, 0.8, 1.0$, respectively.

The magnetic moments expected for low spin configuration have a total spin of $S(\text{Mn}^{2+}) = 0.5$, $S(\text{Mn}^{3+}) = 0$, $S(\text{Mn}^{4+}) = 0.5$, $S(\text{Co}^{2+}) = 0.5$, $S(\text{Co}^{3+}) = 0$, whose magnetic moments are, $\mu = 2\sqrt{S(S+1)} \mu_B$, i.e., $\mu(\text{Mn}^{2+}) = 1.732 \mu_B$, $\mu(\text{Mn}^{3+}) = 0$, $\mu(\text{Mn}^{4+}) = 1.732 \mu_B$, $\mu(\text{Co}^{2+}) = 1.732 \mu_B$, $\mu(\text{Co}^{3+}) = 0$. Furthermore, for high spin configuration $S(\text{Mn}^{2+}) = 2.5$, $S(\text{Mn}^{3+}) = 2.0$, $S(\text{Mn}^{4+}) = 1.5$, $S(\text{Co}^{2+}) = 1.5$, $S(\text{Co}^{3+}) = 2$, whose magnetic moments are $\mu(\text{Mn}^{2+}) = 5.916 \mu_B$, $\mu(\text{Mn}^{3+}) = 4.899 \mu_B$, $\mu(\text{Mn}^{4+}) = 3.873 \mu_B$, $\mu(\text{Co}^{2+}) = 3.873 \mu_B$, $\mu(\text{Co}^{3+}) = 4.899 \mu_B$. Therefore, the magnetic moments for Co and Mn seem to be mainly in the low spin configuration; however, we cannot rule out the presence of some moments in the high spin configuration.

3.9. Oxygen Evolution Reaction (OER)

The samples were also evaluated as electrocatalysts for the oxygen evolution reaction (OER). According to the results of the anodic polarization (Figure 11a), the electrodes presented values of 515 (Ni foam), 342 ($X = 0.0$), 342 ($X = 0.2$), 339 ($X = 0.4$), 337 ($X = 0.6$), 323 ($X = 0.8$), 299 ($X = 1.0$) and 235 (RuO₂/Ni foam benchmark, extracted from reference [95]) mV vs. RHE, respectively, to record a current density $J = 10 \text{ mA cm}^2$. Among the investigated materials, the MnCo₂O₄ ($X = 1.0$) samples displayed the best catalytic activity for OER, i.e., the lowest overpotential because the incorporation of Mn into the structure enhanced the defect concentrations, thus increasing the amount of catalytically active sites, which facilitated the mass transfer process, favoring OER [96]. Moreover, the crystalline size decreased with the increase of manganese content, which indicates that the Co₃O₄ sample ($X = 0.0$) has larger average crystal sizes than the other samples, especially MnCo₂O₄ ($X = 1.0$); thus, Co₃O₄ was the sample that had the highest overpotential. This indicates that the presence of Mn, has a suppressive effect on Co₃O₄ [97]. The obtained values are in agreement with others reported in the literature for Mn_xCo_{3-x}O₄ nanostructures, as shown in Table 5.

Table 5. Comparison of OER performance of nanostructured Mn_xCo_{3-x}O₄ ($0 \leq X \leq 1$) catalysts reported in the literature. Data refer to an overpotential to generate $j = 10 \text{ mA cm}^2$ (η_{10}).

Catalyst	Substrate *	η_{10} (mV vs. RHE)	Tafel Slope (mV dec ⁻¹)	Reference
Mn _x Co _{3-x} O ₄ ($0 \leq X \leq 1$) powders (ágar-ágar)	Ni foam	299	55	This work
Mn _x Co _{3-x} O ₄ ($0 \leq X \leq 2$) powders	Ni foam	327	79	[16]
MnCo ₂ O ₄	GC	510	123	[98]
Co ₃ O ₄ nanoparticles	CFP	361	87.5	[99]
Co ₃ O ₄ Nanosheet	Ni foam	190	103	[100]
Mn _x Co _{3-x} O ₄ ($X = 0.3$)	Ni foam	390	N.R.	[101]
Mn _x Co _{3-x} O ₄ ($X = 0.6$)	GC	365	50.6	[91]
MnCo ₂ O ₄	Ni foam	358	N.R.	[102]
Mn _x Co _{3-x} O ₄ (1:3 ratio)	Ni foam	222	162	[103]
MnCo ₂ O ₄	Ni foam	400	90	[104]
MnCo ₂ O ₄	carbon cloth	400	190	[105]
MnCo ₂ O ₄	GC	510	123	[98]

* CFP (carbon fiber paper); GC (glassy carbon).

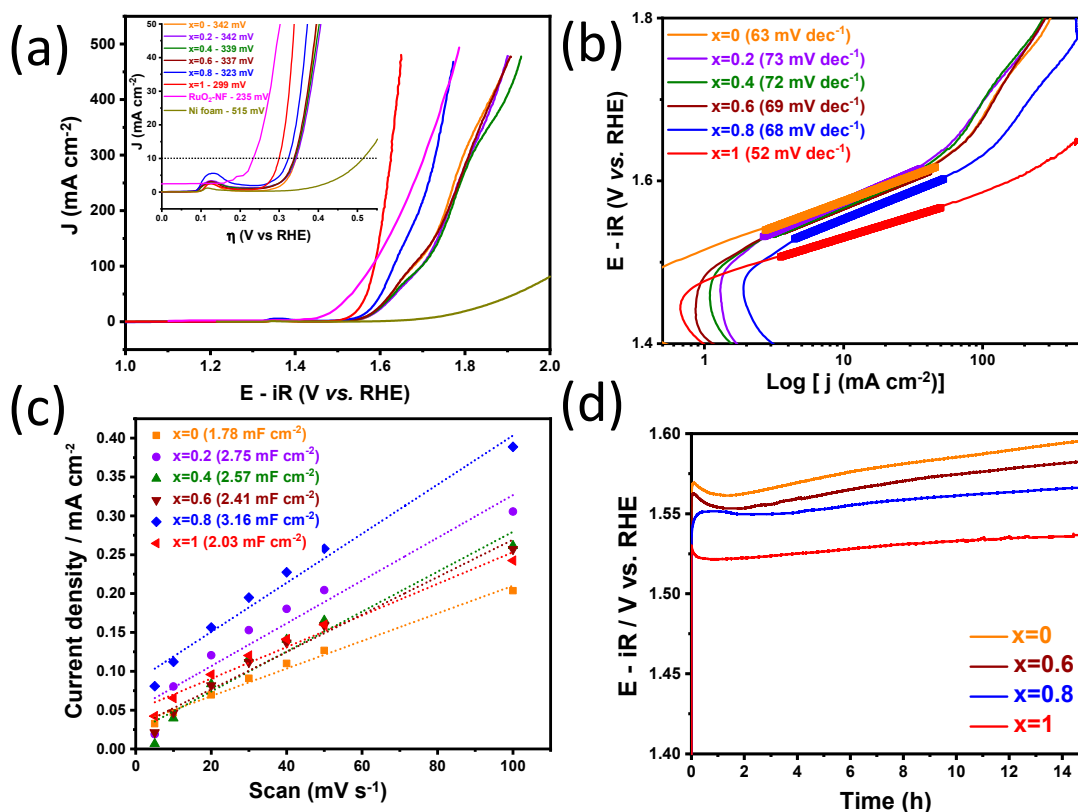


Figure 11. (a) LSV collected at 5 mV s^{-1} in 1 mol L^{-1} KOH for $\text{Mn}_x\text{Co}_{3-x}\text{O}_4$ ($0 \leq X \leq 1$) electrodes, where $X = 0.0$, $X = 0.2$, $X = 0.4$, $X = 0.6$, $X = 0.8$, and $X = 1.0$, and (b) the corresponding Tafel slopes; (c) anodic current (i_a) versus scan rate to determine CDL; (d) chronopotentiometry analysis measured at 10 mA cm^{-2} .

The electrocatalytic kinetics for OER was investigated by the Tafel plots extracted from the LSV (linear sweep voltammetry) curves (Figure 11a), using the Tafel equation ($\eta = a + b \log j$), where b is the Tafel slope, η is the overpotential, j is the current density, and a is a constant. The values of the Tafel slope (Figure 11b) were 63 ($X = 0.0$), 73 ($X = 0.2$), 72 ($X = 0.4$), 69 ($X = 0.6$), 68 ($X = 0.8$), and 52 mV dec^{-1} ($X = 1.0$). Therefore, the results did not follow exactly a sequence like the η_{10} values (Figure 11a), but it can be observed that the electrode based on the MnCo_2O_4 sample ($X = 1.0$) exhibited the best reaction kinetics for OER, as it showed the lowest Tafel slope, which demonstrates a higher efficiency for oxygen evolution. The Tafel slope of 63 mV dec^{-1} for the Co_3O_4 sample ($X = 0.0$) corresponds to slightly slower kinetics, indicating limitation in charge and mass transfer processes compared to the $x = 1.0$ sample. The Co_3O_4 sample was also the one with the highest overpotential, with no distortion in the structure, which reduces defects and consequently the oxygen vacancies [106,107]. These results are consistent with the XPS values as well as the electrochemical impedance spectroscopy. The samples with $X = 0.2$, 0.4 , 0.6 , and 0.8 show values next to 70 mV dec^{-1} , which means much slower kinetics for OER.

All this evidence can be explained by the distortion of the lattice with the increase of the amount of Mn in the Co_3O_4 structure, which changes the electronic charge distribution and increases the disorder in the crystalline system [106–109]. Furthermore, with increasing Mn percentages, the availability of oxygen and flexibility in the lattice is greater, which in turn is related to the M-O bond length [110]. In any case, the samples ($X = 0.2$), ($X = 0.4$), ($X = 0.6$) and ($X = 0.8$) show values of Tafel slope below 80 mV dec^{-1} , and these results indicate the adsorption of intermediate species as the rate-determining step (rds), based on the Krasil'shchikov reaction model for OER in alkaline medium [111,112].

The double-layer capacitance (C_{DL}) can be obtained from the relationship between the anode current density (i_a) and the scan rate (ν), according to ($i_a = \nu \times C_{DL}$) [100].

Figure 11c shows the double-layer capacitance values obtained for the samples: 1.78 ($X = 0.0$), 2.75 ($X = 0.2$), 2.57 ($X = 0.4$), 2.41 ($X = 0.6$), 3.16 ($X = 0.8$), and 2.03 mF cm^{-2} ($X = 1.0$). These results suggest that the largest number of active sites is organized on the electrode surfaces. Although among the samples of this series, the one with $X = 0.8$ had the second lowest performance for OER, it displays the highest C_{DL} value, which may be linked to the high amount of oxygen vacancies that improves the absorption of reactive species (like OH^-) [113]. For the samples ($X = 0.2$), ($X = 0.4$), and ($X = 0.6$), the values of 2.75, 2.57, and 2.41 mF cm^{-2} , respectively, are consistent with the XPS data (Figure 9b), where the species in the lowest oxidation state, Mn^{2+} , represented the largest fraction of the total species present on the surface, with a relative fraction ranging from 0.42–0.51 among the samples. However, even with a low C_{DL} value for the sample ($X = 1.0$), the presence of Mn ions in the structure is essential for superior electrocatalytic properties. This was proven by the best overpotential extracted from the LSV curves (Figure 11a) and the XPS data (Figure 9c), as the substitution of Mn in spinel oxide cobalt occurs selectively in the (Co^{3+}) lattices, and the energy required for Mn^{2+} to substitute Co^{3+} is lower than that of Co^{2+} , [114]. Moreover, Mn^{+2} , Mn^{+3} , and Mn^{+4} have ionic radii of 0.80, 0.66, and 0.60 Å, respectively, and the ratios of Mn^{+2} and Mn^{+3} are larger than that of Co^{3+} (0.63 Å). Therefore, Mn doping results in the expansion of the Co_3O_4 lattice, generating defects, which influences the mass diffusion and charge transfer properties, contributing to oxygen-ion vacancies, which are consistent with the O_2/O_1 ratio that was highest for the MnCo_2O_4 sample ($X = 1.0$), with a value of 0.940 [108,109,115,116].

Durability is another important indicator of catalytic performance. The stability of the electrocatalysts was evaluated by chronopotentiometry. Tests were performed at a current density of 10 mA cm^{-2} for 15 h. According to the curves shown in Figure 11d, it can be seen that the samples ($X = 0$) and ($X = 0.6$) exhibited a potential decrease until about 2 h, but then they remained stable, whereas for the samples ($X = 0.8$) and ($X = 1.0$), the potential was practically stable for the entire time period tested. In general, all samples showed satisfactory stability over 15 h of testing [117].

3.10. Electrochemical Impedance Spectroscopy (EIS)

The electrocatalytic activity also was investigated by electrochemical impedance spectroscopy (EIS). The EIS spectra of all samples were collected at 1.4 V vs. RHE. As seen in the Bode plots (Figure 12b), the OER is composed of complex processes involving electrosorption of intermediate species during the reaction progress. This suggests an equivalent circuit model (ECM) able to describe these processes [118,119] that is composed of R_s (uncompensated solution resistance), R_p (polarization resistance, which denotes the overall rate of the OER), Q_{DL} (double-layer pseudo-capacitance), R_{ad} (resistance associated with adsorption of intermediate species), and Q_{ad} (pseudo-capacitance of these species throughout the reaction). A constant phase element (Q) was used to model an imperfect capacitor, and its impedance was obtained by:

$$Z_Q = (Q(i\omega)^n)^{-1} \quad (1)$$

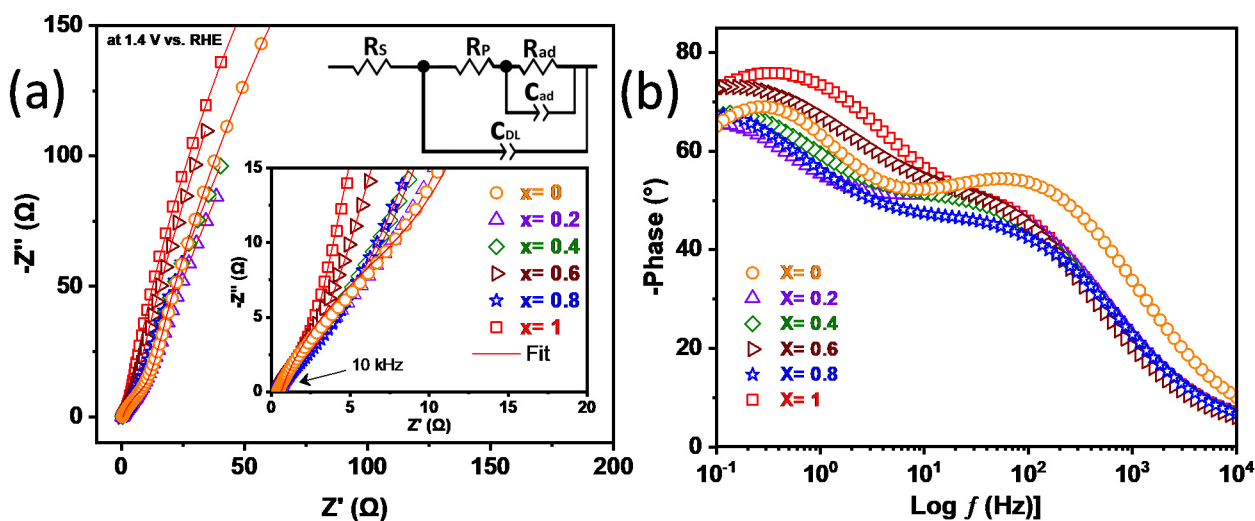


Figure 12. EIS—Nyquist (a) and Bode (b) plots for the tested electrocatalysts.

Then, the values were used to calculate true capacitance (C_{DL} or C_{-ad}) by:

$$C = R^{(1-n)/n} Q^{1/n} \quad (2)$$

In Figure 12a, the impedance of the electrodes is composed of two incomplete semi-circles. The first is attributed to the polarization process (charge transfer), and the second indicates limitations on mass transfer processes, related to the intermediate species adsorption process [120]. For the electrodes, the obtained R_p values were consistent with the OER performance, i.e., the $X = 1.0$ sample showed the lowest value (6.02Ω), followed by $X = 0.8$ (9.70Ω). The other samples revealed R_p values very close, but the result was expected as their overpotential values were close. The C_{DL} values varied slightly (Table 6) due to the oxidation peak shown in Figure 11a. The $R_{ad}C_{ad}$ loop associated with relaxation, which was attributed to the adsorbed intermediate species, revealed the difficulty of these electrodes to work in the diffusive processes observed at low frequencies. The high R_{ad} ($>1100 \Omega$) values displayed by the electrodes in those low frequency (>1 Hz) confirm that the adsorption of intermediates should be a rate-limiting step as predicted by Tafel analysis (Figure 11b) [118,121]. The values obtained from the fitting of the spectra are listed in Table 6.

Table 6. EIS—Results of fitting of the impedance spectra reported in Figure 12.

Sample	R_s (Ω)	R_p (Ω)	C_{DL} (mF)	R_{ad} (Ω)	C_{-ad} (mF)
$X = 1.0$	0.41	6.02	2.55	1292	6.07
$X = 0.0$	0.62	28.15	1.49	1276	3.36
$X = 0.2$	0.48	30.69	6.01	1917	8.47
$X = 0.4$	0.52	20.29	4.55	1374	8.86
$X = 0.6$	0.43	19.21	3.88	2149	10.34
$X = 0.8$	0.46	9.70	8.27	1135	11.77

4. Conclusions

The $Mn_xCo_{3-x}O_4$ ($0 \leq X \leq 1$) samples were synthesized by the proteic sol-gel method (green synthesis) using Agar-Agar as a polymerizing agent in order to investigate their structural, optical, magnetic, and electrochemical properties. X-ray diffraction indicated for all samples the obtainment of the pure cubic phase without any secondary phase, which was also confirmed from Raman, TEM, FT-IR, and UV-Vis studies. Regarding the magnetic measurements, it was observed for all samples a magnetization in a certain field increasing with the Mn concentration, which is typical of a paramagnetic behavior. From the XPS analysis, the species in the Mn^{2+} oxidation state represented the largest fraction of the

total species present on the surface, and as the amount of Mn increased, the O_2/O_1 ratio also increased, reaching a value of 0.940 for the sample $MnCo_2O_4$ ($X = 1.0$). For OER, the same sample exhibited the best catalytic activity when compared with the others, with an overpotential of 299 mV, which is lower than those of noble metal electrocatalysts reported in the literature. In addition, the samples showed superior long-term stability for efficient water oxidation activities at $J = 10 \text{ mA/cm}^2$ per 15 h. Thus, it can be concluded that proteic sol-gel synthesis is an excellent method to produce nanosized mixed-valence oxides $Mn_xCo_{3-x}O_4$ for the fabrication of electrodes for water electrolysis.

Author Contributions: J.R.D.S.: Conceptualization, Investigation, Methodology, Software, Data curation, Writing—original draft preparation. R.R.A.: Software, Data curation, Writing—original draft preparation. T.R.S.: Software, Data curation. V.D.S.: Software, Data curation, Writing—original draft preparation. D.A.M.: Writing—review and editing. F.J.A.L.: Software, Data curation, Writing—original draft preparation. M.A.M.T.: Software, Data curation, Writing—review and editing. D.T.: Writing—review and editing. U.U.G.: Writing—review and editing, supervision. All authors have read and agreed to the published version of the manuscript.

Funding: CAPES—Finance code 01.

Institutional Review Board Statement: Not applicable.

Informed Consent Statement: Not applicable.

Data Availability Statement: The study did not report any data.

Acknowledgments: The authors thank the Coordination for the Improvement of Higher Education Personnel (CAPES, Finance Code 001). This work was funded by Public Call No. 01/2021 Produtividade em Pesquisa PROPESQ/PRPG/UFPB Proposal Code PVF 14860-2021. Uílame Umbelino Gomes—(CNPQ-Level 1B Research Productivity Fellowship, N.308894/2021-9). Rafael A. Raimundo acknowledges Paraíba State Research Foundation (FAPESQ) for the financial support through the Postdoctoral Fellowship in the country—BLD—PDRP (Public notice N° 07/2021, program 22210.19.573.5011.1680). Francisco J. A. Loureiro expresses his gratitude to the projects CEECIND/02797/2020, PTDC/CTM-CTM/2156/2020, UIDB/00481/2020 and UIDP/00481/2020 from Fundação para a Ciência e a Tecnologia (FCT) and CENTRO-01-0145-FEDER-022083—Centro Portugal Regional Operational Programme (Centro2020), under the PORTUGAL 2020 Partnership Agreement, through the European Regional Development Fund (ERDF). Vinícius D. Silva thanks the national research Council (CNPq, Process No. 202290/2020-4). Daniel A. Macedo and Marco A. Morales acknowledge CNPq/Brazil (309430/2019-4 and 313337/2018-7) for the financial support given. We thank Tatiane Oliveira dos Santos at LABMIC-UFG for providing TEM images.

Conflicts of Interest: The authors declare no conflict of interest.

References

1. Roy, A.; Jadhav, H.S.; Cho, M.; Seo, J.G. Electrochemical deposition of self-supported bifunctional copper oxide electrocatalyst for methanol oxidation and oxygen evolution reaction. *J. Ind. Eng. Chem.* **2019**, *76*, 515–523. [[CrossRef](#)]
2. Sivakumar, P.; Subramanian, P.; Maiyalagan, T.; Gedanken, A.; Schechter, A. Ternary nickel–cobalt–manganese spinel oxide nanoparticles as heterogeneous electrocatalysts for oxygen evolution and oxygen reduction reaction. *Mater. Chem. Phys.* **2019**, *229*, 190–196. [[CrossRef](#)]
3. Jiang, B.; Kim, J.; Guo, Y.; Wu, K.C.W.; Alshehri, S.M.; Ahamad, T.; Alhokbany, N.; Henzie, J.; Yamachi, Y. Efficient oxygen evolution on mesoporous IrO_x nanosheets. *Catal. Sci. Technol.* **2019**, *9*, 3697–3702. [[CrossRef](#)]
4. Tu, Q.; Mo, J.; Liu, Z.; Gong, C.; Fan, Y. Using green finance to counteract the adverse effects of COVID-19 pandemic on renewable energy investment—The case of offshore wind power in China. *Energy Policy* **2021**, *158*, 112542. [[CrossRef](#)] [[PubMed](#)]
5. Iskandarova, M.; Dembek, A.; Fraaije, M.; Matthews, W.; Stasik, A.; Wittmayer, J.M.; Sovacool, B.K. Who finances renewable energy in Europe? Examining temporality, authority and contestation in solar and wind subsidies in Poland, the Netherlands and the United Kingdom. *Energy Strateg. Rev.* **2021**, *38*, 100730. [[CrossRef](#)]
6. Cousse, J. Still in love with solar energy? Installation size, affect, and the social acceptance of renewable energy technologies. *Renew. Sustain. Energy Rev.* **2021**, *145*, 111107. [[CrossRef](#)]
7. Sayed, E.T.; Wilberforce, T.; Elsaid, K.; Rabaia, M.K.H.; Abdelkareem, M.A.; Chae, K.-J.; Olabi, A. A critical review on environmental impacts of renewable energy systems and mitigation strategies: Wind, hydro, biomass and geothermal. *Sci. Total Environ.* **2021**, *766*, 144505. [[CrossRef](#)]

8. Rashidi, S.; Karimi, N.; Sunden, B.; Kim, K.C.; Olabi, A.G.; Mahian, O. Progress and challenges on the thermal management of electrochemical energy conversion and storage technologies: Fuel cells, electrolysers, and supercapacitors. *Prog. Energy Combust. Sci.* **2022**, *88*, 100966. [[CrossRef](#)]
9. Tomon, C.; Sarawutanukul, S.; Phattharasupakun, N.; Duangdangchote, S.; Chomkhundtod, P.; Kidkhunthod, P.; Sawangphruk, M. Insight into photoelectrocatalytic mechanisms of bifunctional cobaltite hollow-nanofibers towards oxygen evolution and oxygen reduction reactions for high-energy zinc-air batteries. *Electrochim. Acta* **2021**, *392*, 139022. [[CrossRef](#)]
10. Vazhayil, A.; Vazhayal, L.; Thomas, J.; Ashok, C.S.; Thomas, N. A comprehensive review on the recent developments in transition metal-based electrocatalysts for oxygen evolution reaction. *Appl. Surf. Sci. Adv.* **2021**, *6*, 100184. [[CrossRef](#)]
11. Anwar, S.; Khan, F.; Zhang, Y.; Djire, A. Recent development in electrocatalysts for hydrogen production through water electrolysis. *Int. J. Hydrogen Energy* **2021**, *46*, 32284–32317. [[CrossRef](#)]
12. Lourenço, A.D.A.; Silva, V.D.; da Silva, R.; Silva, U.C.; Chesman, C.; Salvador, C.; Simões, T.; de Macedo, D.A.; da Silva, F.F. Metal-organic frameworks as template for synthesis of Mn³⁺/Mn⁴⁺ mixed valence manganese cobaltites electrocatalysts for oxygen evolution reaction. *J. Colloid Interface Sci.* **2021**, *582*, 124–136. [[CrossRef](#)] [[PubMed](#)]
13. Song, X.-Z.; Zhang, N.; Liu, F.; Wang, Z.-H.; Zhu, W.-Y.; Zhang, G.-Z.; Niu, Z.-Y.; Wang, X.-F.; Tan, Z. Spontaneously engineering heterogeneous interface of silver nanoparticles on α -Co(OH)₂ for boosting electrochemical oxygen evolution. *J. Alloys Compd.* **2021**, *873*, 159766. [[CrossRef](#)]
14. Zhang, T.; Meng, Y.-L.; Zhao, Y.-H.; Ni, J.-C.; Pan, Y.; Dai, Y.; Tan, Z.; Wang, X.-F.; Song, X.-Z. Boosting oxygen evolution electrocatalysis of high-entropy hydroxide by high-valency nickel regulation. *Chem. Commun.* **2022**, *58*, 7682–7685. [[CrossRef](#)]
15. Jamesh, M.I.; Sun, X. Recent progress on earth abundant electrocatalysts for oxygen evolution reaction (OER) in alkaline medium to achieve efficient water splitting—A review. *J. Power Sources* **2018**, *400*, 31–68. [[CrossRef](#)]
16. Lankauf, K.; Cysewska, K.; Karczewski, J.; Mielewczyk-Gryń, A.; Górnicka, K.; Cempura, G.; Chen, M.; Jasiński, P.; Molin, S. Mn_xCo_{3-x}O₄ spinel oxides as efficient oxygen evolution reaction catalysts in alkaline media. *Int. J. Hydrogen Energy* **2020**, *45*, 14867–14879. [[CrossRef](#)]
17. Tao, L.; Guo, P.; Zhu, W.; Li, T.; Zhou, X.; Fu, Y.; Yu, C.; Ji, H. Highly efficient mixed-metal spinel cobaltite electrocatalysts for the oxygen evolution reaction. *Chin. J. Catal.* **2020**, *41*, 1855–1863. [[CrossRef](#)]
18. Liu, Q.; Chen, Z.; Yan, Z.; Wang, Y.; Wang, E.; Wang, S.; Wang, S.; Sun, G. Crystal-Plane-Dependent Activity of Spinel Co₃O₄ Towards Water Splitting and the Oxygen Reduction Reaction. *ChemElectroChem* **2018**, *5*, 1080–1086. [[CrossRef](#)]
19. Leng, M.; Huang, X.; Xiao, W.; Ding, J.; Liu, B.; Du, Y.; Xue, J. Enhanced oxygen evolution reaction by Co-O-C bonds in rationally designed Co₃O₄/graphene nanocomposites. *Nano Energy* **2017**, *33*, 445–452. [[CrossRef](#)]
20. Lee, E.; Jang, J.H.; Kwon, Y.U. Composition effects of spinel Mn_xCo_{3-x}O₄ nanoparticles on their electrocatalytic properties in oxygen reduction reaction in alkaline media. *J. Power Sources* **2015**, *273*, 735–741. [[CrossRef](#)]
21. Rios, E.; Chartier, P.; Gautier, J.-L. Oxygen evolution electrocatalysis in alkaline medium at thin Mn_xCo_{3-x}O₄ (0 ≤ x ≤ 1) spinel films on glass/SnO₂: F prepared by spray pyrolysis. *Solid State Sci.* **1999**, *1*, 267–277. [[CrossRef](#)]
22. Shi, C.; Ullah, S.; Li, K.; Wang, W.; Zhang, R.; Pan, L.; Zhang, X.; Zou, J.-J. Low-temperature synthesis of ultrasmall spinel Mn_xCo_{3-x}O₄ nanoparticles for efficient oxygen reduction. *Chin. J. Catal.* **2020**, *41*, 1818–1825. [[CrossRef](#)]
23. Shen, Z.; Rong, J.; Yu, X. Mn_xCo_{3-x}O₄ spinel coatings: Controlled synthesis and high temperature oxidation resistance behavior. *Ceram. Int.* **2020**, *46*, 5821–5827. [[CrossRef](#)]
24. Li, D.; Kang, Z.; Sun, H.; Wang, Y.; Xie, H.; Liu, J.; Zhu, J. A bifunctional Mn_xCo_{3-x}O₄-decorated separator for efficient Li-Li-O₂ batteries: A novel strategy to promote redox coupling and inhibit redox shuttling. *Chem. Eng. J.* **2022**, *428*, 131105. [[CrossRef](#)]
25. Wang, Y.; Yang, Y.; Jia, S.; Wang, X.; Lyu, K.; Peng, Y.; Zheng, H.; Wei, X.; Ren, H.; Xiao, L.; et al. Synergistic Mn-Co catalyst outperforms Pt on high-rate oxygen reduction for alkaline polymer electrolyte fuel cells. *Nat. Commun.* **2019**, *10*, 1506. [[CrossRef](#)]
26. Talic, B.; Hendriksen, P.V.; Wiik, K.; Lein, H.L. Thermal expansion and electrical conductivity of Fe and Cu doped MnCo₂O₄ spinel. *Solid State Ion.* **2018**, *326*, 90–99. [[CrossRef](#)]
27. Zhao, Q.; Yan, Z.; Chen, C.; Chen, J. Spinels: Controlled Preparation, Oxygen Reduction/Evolution Reaction Application, and beyond. *Chem. Rev.* **2017**, *117*, 10121–10211. [[CrossRef](#)]
28. Mandal, B.; Mitra, P. Grain growth correlated complex impedance spectroscopy, modulus spectroscopy and carrier hopping mechanism in MnCo₂O₄, Influence of sintering temperature. *Mater. Chem. Phys.* **2020**, *251*, 123095. [[CrossRef](#)]
29. Tajik, S.; Dubal, D.P.; Gomez-Romero, P.; Yadegari, A.; Rashidi, A.; Nasernejad, B.; Inamuddin; Asiri, A.M. Nanostructured mixed transition metal oxides for high performance asymmetric supercapacitors: Facile synthetic strategy. *Int. J. Hydrogen Energy* **2017**, *42*, 12384–12395. [[CrossRef](#)]
30. Yang, H.; Hu, F.; Zhang, Y.; Shi, L.; Wang, Q. Controlled synthesis of porous spinel cobalt manganese oxides as efficient oxygen reduction reaction electrocatalysts. *Nano Res.* **2016**, *9*, 207–213. [[CrossRef](#)]
31. Lavela, P.; Tirado, J.L.; Vidal-Abarca, C. Sol-gel preparation of cobalt manganese mixed oxides for their use as electrode materials in lithium cells. *Electrochim. Acta* **2007**, *52*, 7986–7995. [[CrossRef](#)]
32. Park, K.R.; Jeon, J.E.; Ali, G.; Ko, Y.-H.; Lee, J.; Han, H.; Mhin, S. Oxygen evolution reaction of Co-Mn-O electrocatalyst prepared by solution combustion synthesis. *Catalysts* **2019**, *9*, 564. [[CrossRef](#)]
33. Zhao, T.; Gadipelli, S.; He, G.; Ward, M.J.; Do, D.; Zhang, P.; Guo, Z. Tunable Bifunctional Activity of Mn_xCo_{3-x}O₄ Nanocrystals Decorated on Carbon Nanotubes for Oxygen Electrocatalysis. *ChemSusChem* **2018**, *11*, 1295–1304. [[CrossRef](#)]

34. Wei, C.; Feng, Z.; Scherer, G.G.; Barber, J.; Shao-Horn, Y.; Xu, Z.J. Cations in Octahedral Sites: A Descriptor for Oxygen Electrocatalysis on Transition-Metal Spinels. *Adv. Mater.* **2017**, *29*, 1606800. [[CrossRef](#)]
35. Bobruk, M.; Brylewska, K.; Durczak, K.; Wojciechowski, K.; Adamczyk, A.; Brylewski, T. Synthesis of manganese-cobalt spinel via wet chemistry methods and its properties. *Ceram. Int.* **2017**, *43*, 15597–15609. [[CrossRef](#)]
36. Ríos, E.; Peña, O.; Guizouarn, T.; Gautier, J.-L. Thin films of Co_3O_4 , MnCo_2O_4 and their solid solution as electrocatalyst: Study of their magnetic properties. *Phys. Status Solidi* **2004**, *1*, S108–S111. [[CrossRef](#)]
37. Rebekah, A.; Anantharaj, S.; Viswanthan, C.; Ponpandian, N. ScienceDirect Zn-substituted MnCo_2O_4 nanostructure anchored over rGO for boosting the electrocatalytic performance towards methanol oxidation and oxygen evolution reaction (OER). *Int. J. Hydrogen Energy* **2020**, *45*, 14713–14727. [[CrossRef](#)]
38. Itteboina, R.; Sau, T.K. Sol-gel synthesis and characterizations of morphology-controlled Co_3O_4 particles. *Mater. Today Proc.* **2019**, *9*, 458–467. [[CrossRef](#)]
39. Guo, J.; Chen, L.; Zhang, X.; Jiang, B.; Ma, L. Sol-gel synthesis of mesoporous Co_3O_4 octahedra toward high-performance anodes for lithium-ion batteries. *Electrochim. Acta* **2014**, *129*, 410–415. [[CrossRef](#)]
40. Silva, R.M.; Raimundo, R.A.; Fernandes, W.V.; Torres, S.M.; Silva, V.D.; Grilo, J.P.; Morales, M.A.; Macedo, D.A. Proteic sol-gel synthesis, structure and magnetic properties of Ni/NiO core-shell powders. *Ceram. Int.* **2018**, *44*, 6152–6156. [[CrossRef](#)]
41. Amri, A.; Jiang, Z.T.; Pryor, T.; Yin, C.Y.; Djordjevic, S. Developments in the synthesis of flat plate solar selective absorber materials via sol-gel methods: A review. *Renew. Sustain. Energy Rev.* **2014**, *36*, 316–328. [[CrossRef](#)]
42. Nair, P.A.K.; Vasconcelos, W.L.; Paine, K.; Calabria-Holley, J. A review on applications of sol-gel science in cement. *Constr. Build. Mater.* **2021**, *291*, 123065. [[CrossRef](#)]
43. da Silva, M.V.; Fajardo, H.V.; Rodrigues, T.S.; e Silva, F.A.; Bergamaschi, V.S.; Dias, A.; Siqueira, K.P. Synthesis of NiMoO_4 ceramics by proteic sol-gel method and investigation of their catalytic properties in hydrogen production. *Mater. Chem. Phys.* **2021**, *262*, 124301. [[CrossRef](#)]
44. Pimentel, P.M.; Lima, S.V.M.; Costa, A.F.; Câmara, M.S.C.; Carregosa, J.D.C.; Oliveira, R.M.P.B. Gelatin synthesis and color properties of (La, Pr, Nd) lanthanide aluminates. *Ceram. Int.* **2017**, *43*, 6592–6596. [[CrossRef](#)]
45. Santos, J.R.; Loureiro, F.J.; Grilo, J.P.; Silva, V.D.; Simões, T.A.; Fagg, D.P.; Macedo, D.A. Understanding the cathodic polarisation behaviour of the misfit $[\text{Ca}_2\text{CoO}_{3-\delta}]_q[\text{CoO}_2]$ (C349) as oxygen electrode for IT-SOFC. *Electrochim. Acta* **2018**, *285*, 214–220. [[CrossRef](#)]
46. Ferreira, L.S.; Silva, T.R.; Silva, V.D.; Simões, T.A.; Araújo, A.J.; Morales, M.A.; Macedo, D.A. Proteic sol-gel synthesis, structure and battery-type behavior of Fe-based spinels (MFe_2O_4 , M = Cu, Co, Ni). *Adv. Powder Technol.* **2020**, *31*, 604–613. [[CrossRef](#)]
47. Santos, J.V.A.; Macedo, M.A.; Cunha, F.; Sasaki, J.M.; Duque, J.G.S. $\text{BaFe}_{12}\text{O}_{19}$ thin film grown by an aqueous sol-gel process. *Microelectron. J.* **2003**, *34*, 565–567. [[CrossRef](#)]
48. Ferreira, L.S.; Silva, T.R.; Santos, J.R.; Silva, V.D.; Raimundo, R.A.; Morales, M.A.; Macedo, D.A. Structure, magnetic behavior and OER activity of CoFe_2O_4 powders obtained using agar-agar from red seaweed (Rhodophyta). *Mater. Chem. Phys.* **2019**, *237*, 121847. [[CrossRef](#)]
49. Rees, D.A. Structure, Conformation, and Mechanism in the Formation of Polysaccharide Gels and Networks. *Adv. Carbohydr. Chem. Biochem.* **1969**, *24*, 267–332. [[CrossRef](#)]
50. Rhein-Knudsen, N.; Ale, M.T.; Ajallouei, F.; Yu, L.; Meyer, A.S. Rheological properties of agar and carrageenan from Ghanaian red seaweeds. *Food Hydrocoll.* **2017**, *63*, 50–58. [[CrossRef](#)]
51. Kartik, A.; Akhil, D.; Lakshmi, D.; Gopinath, K.P.; Arun, J.; Sivaramakrishnan, R.; Pugazhendhi, A. A critical review on production of biopolymers from algae biomass and their applications. *Bioresour. Technol.* **2021**, *329*, 124868. [[CrossRef](#)] [[PubMed](#)]
52. Malagurski, I.; Levic, S.; Nestic, A.; Mitric, M.; Pavlovic, V.; Dimitrijevic-Brankovic, S. Mineralized agar-based nanocomposite films: Potential food packaging materials with antimicrobial properties. *Carbohydr. Polym.* **2017**, *175*, 55–62. [[CrossRef](#)]
53. Francavilla, M.; Pineda, A.; Lin, C.S.; Franchi, M.; Trotta, P.; Romero, A.A.; Luque, R. Natural porous agar materials from macroalgae. *Carbohydr. Polym.* **2013**, *92*, 1555–1560. [[CrossRef](#)]
54. Arnott, S.; Fulmer, A.; Scott, W.E.; Dea, I.C.M.; Moorhouse, R.; Rees, D.A. The Agarose Double Helix and Its Function in Agarose Gel Structure. *J. Mol. Biol.* **1974**, *90*, 269–284. [[CrossRef](#)]
55. Pradhan, B.; Bhuyan, P.P.; Patra, S.; Nayak, R.; Behera, P.K.; Behera, C.; Behera, A.K.; Ki, J.-S.; Jena, M. Beneficial effects of seaweeds and seaweed-derived bioactive compounds: Current evidence and future prospective. *Biocatal. Agric. Biotechnol.* **2022**, *39*, 102242. [[CrossRef](#)]
56. Picard, J.P.; Baud, G.; Besse, J.P.; Chevalier, R. Croissance cristalline et étude structurale de Co_3O_4 . *J. Less-Common Met.* **1980**, *75*, 99–104. [[CrossRef](#)]
57. Dang, W.; Tang, X.; Wang, W.; Yang, Y.; Li, X.; Huang, L.; Zhang, Y. Micro-nano $\text{NiO-MnCo}_2\text{O}_4$ heterostructure with optimal interfacial electronic environment for high performance and enhanced lithium storage kinetics. *Dalton Trans.* **2020**, *49*, 10994–11004. [[CrossRef](#)]
58. Restovic, A.; Ríos, E.; Barbato, S.; Ortiz, J.; Gautier, J. Oxygen reduction in alkaline medium at thin $\text{Mn}_x\text{Co}_{3-x}\text{O}_4$ ($0 \leq x \leq 1$) spinel films prepared by spray pyrolysis. Effect of oxide cation composition on the reaction kinetics. *J. Electroanal. Chem.* **2002**, *522*, 141–151. [[CrossRef](#)]
59. Raj, S.; Anantharaj, S.; Kundu, S.; Roy, P. In Situ Mn-Doping-Promoted Conversion of $\text{Co}(\text{OH})_2$ to Co_3O_4 as an Active Electrocatalyst for Oxygen Evolution Reaction. *ACS Sustain. Chem. Eng.* **2019**, *7*, 9690–9698. [[CrossRef](#)]

60. Hu, H.; Cai, S.; Li, H.; Huang, L.; Shi, L.; Zhang, D. In Situ DRIFTS Investigation of the Low-Temperature Reaction Mechanism over Mn-Doped Co_3O_4 for the Selective Catalytic Reduction of NO with NH_3 . *J. Phys. Chem. C* **2015**, *119*, 22924–22933. [[CrossRef](#)]
61. Wyckoff, R.W.G. *Crystal Structures*, 1st ed.; Interscience: New York, NY, USA; London, UK; Sydney, Australia, 1963; Volume 1. [[CrossRef](#)]
62. Dutta, A. *Fourier Transform Infrared Spectroscopy*; Elsevier Inc.: Amsterdam, The Netherlands, 2017; Volume 2. [[CrossRef](#)]
63. Ai, L.H.; Jiang, J. Rapid synthesis of nanocrystalline Co_3O_4 by a microwave-assisted combustion method. *Powder Technol.* **2009**, *195*, 11–14. [[CrossRef](#)]
64. Yin, J.; Cao, H.; Lu, Y. Self-assembly into magnetic Co_3O_4 complex nanostructures as peroxidase. *J. Mater. Chem.* **2012**, *22*, 527–534. [[CrossRef](#)]
65. Tholkappian, R.; Naveen, A.N.; Sumithra, S.; Vishista, K. Investigation on spinel MnCo_2O_4 electrode material prepared via controlled and uncontrolled synthesis route for supercapacitor application. *J. Mater. Sci.* **2015**, *50*, 5833–5843. [[CrossRef](#)]
66. Petit, S.; Madejova, J. *Fourier Transform Infrared Spectroscopy*, 2nd ed.; Elsevier Ltd.: Amsterdam, The Netherlands, 2013; Volume 5. [[CrossRef](#)]
67. Basumatary, K.; Daimary, P.; Das, S.K.; Thapa, M.; Singh, M.; Mukherjee, A.; Kumar, S. Lagerstroemia speciosa fruit-mediated synthesis of silver nanoparticles and its application as filler in agar based nanocomposite films for antimicrobial food packaging. *Food Packag. Shelf Life* **2018**, *17*, 99–106. [[CrossRef](#)]
68. Naveen, A.N.; Selladurai, S. Investigation on physicochemical properties of Mn substituted spinel cobalt oxide for supercapacitor applications. *Electrochim. Acta* **2014**, *125*, 404–414. [[CrossRef](#)]
69. Xie, L.; Li, K.; Sun, G.; Hu, Z.; Lv, C.; Wang, J.; Zhang, C. Preparation and electrochemical performance of the layered cobalt oxide (Co_3O_4) as supercapacitor electrode material. *J. Solid State Electrochem.* **2013**, *17*, 55–61. [[CrossRef](#)]
70. Habibi, M.H.; Bagheri, P. Enhanced photo-catalytic degradation of naphthol blue black on nano-structure MnCo_2O_4 , charge separation of the photo-generated electron–hole pair. *J. Mater. Sci. Mater. Electron.* **2017**, *28*, 289–294. [[CrossRef](#)]
71. Uke, S.J.; Chaudhari, G.N.; Kumar, Y.; Mardikar, S.P. Tri-Ethanolamine-Ethoxylate assisted hydrothermal synthesis of nanostructured MnCo_2O_4 with superior electrochemical performance for high energy density supercapacitor application. *Mater. Today Proc. J.* **2021**, *43*, 2792–2799. [[CrossRef](#)]
72. Mu, J.; Zhang, L.; Zhao, M.; Wang, Y. Co_3O_4 nanoparticles as an efficient catalase mimic: Properties, mechanism and its electrocatalytic sensing application for hydrogen peroxide. *J. Mol. Catal. A Chem.* **2013**, *378*, 30–37. [[CrossRef](#)]
73. Deng, J.; Cheng, Y.-Q.; Lu, Y.-A.; Crittenden, J.C.; Zhou, S.-Q.; Gao, N.-Y.; Li, J. Mesoporous Manganese Cobaltite Nanocages as Effective and Reusable Heterogeneous Peroxymonosulfate Activators for Carbamazepine Degradation. *Chem. Eng. J.* **2017**, *330*, 505–517. [[CrossRef](#)]
74. Mohamed, M.A.; Jaafar, J.; Ismail, A.F.; Othman, M.H.D.; Rahman, M.A. *Fourier Transform Infrared (FTIR) Spectroscopy*; Elsevier B.V.: Amsterdam, The Netherlands, 2017. [[CrossRef](#)]
75. Rojas, R.M.; Vila, E.; García, O.; de Vidales, J.L.M. Thermal Behaviour and Reactivity of Manganese Cobaltites $\text{Mn}_x\text{Co}_{3-x}\text{O}_4$ ($0.0 < x < 1.0$) obtained at Low Temperature. *J. Mater. Chem.* **1994**, *4*, 1635–1639. [[CrossRef](#)]
76. Zhang, N.; Shi, J.; Mao, S.S.; Guo, L. Co_3O_4 quantum dots: Reverse micelle synthesis and visible-light-driven photocatalytic overall water splitting. *Chem. Commun.* **2014**, *50*, 2002–2004. [[CrossRef](#)] [[PubMed](#)]
77. Barreca, D.; Massignan, C.; Daolio, S.; Fabrizio, M.; Piccirillo, C.; Armelao, L.; Tondello, E. Composition and Microstructure of Cobalt Oxide Thin Films Obtained from a Novel Cobalt (II) Precursor by Chemical Vapor Deposition. *Chem. Mater.* **2001**, *13*, 588–593. [[CrossRef](#)]
78. Cook, J.G.; Meer, M.P.V.D. The Optical Properties of Sputtered Co_3O_4 Films. *Thin Solid Films* **1986**, *144*, 165–176. [[CrossRef](#)]
79. SSun, C.; Yang, J.; Dai, Z.; Wang, X.; Zhang, Y.; Li, L.; Chen, P.; Huang, W.; Dong, X. Nanowires assembled from MnCo_2O_4 @C nanoparticles for water splitting and all-solid-state supercapacitor. *Nano Res.* **2016**, *9*, 1300–1309. [[CrossRef](#)]
80. Saravanakumar, B.; Ravi, G.; Ganesh, V.; Guduru, R.K.; Yuvakkumar, R. MnCo_2O_4 nanosphere synthesis for electrochemical applications. *Mater. Sci. Energy Technol.* **2018**, *2*, 130–138. [[CrossRef](#)]
81. Hadjiev, V.G.; Iliev, M.; Vergilov, I.V. The Raman spectra of Co_3O_4 . *J. Phys. C Solid State Phys.* **1988**, *21*, L199–L201. [[CrossRef](#)]
82. Jiang, J.; Li, L. Synthesis of sphere-like Co_3O_4 nanocrystals via a simple polyol route. *Mater. Lett.* **2007**, *61*, 4894–4896. [[CrossRef](#)]
83. Zhao, Y.; Li, Y.; Ma, C.; Shao, Z. Micro-/nano-structured hybrid of exfoliated graphite and Co_3O_4 nanoparticles as high-performance anode material for Li-ion batteries. *Electrochim. Acta* **2016**, *213*, 98–106. [[CrossRef](#)]
84. Du, S.; Ren, Z.; Qu, Y.; Wu, J.; Xi, W.; Zhu, J.; Fu, H. Co_3O_4 nanosheets as the high-performance catalyst for oxygen evolution proceeding via the twice two-electron process. *Chem. Commun.* **2016**, *52*, 6705–6708. [[CrossRef](#)]
85. Islam, M.N.; Pradhan, A.; Kumar, S. Effects of crystallite size distribution on the Raman-scattering profiles of silicon nanostructures. *J. Appl. Phys.* **2005**, *98*, 024309. [[CrossRef](#)]
86. Zhang, S.Y.; Yang, Y.Y.; Zheng, Y.Q.; Zhu, H.L. Ag-doped Co_3O_4 catalyst derived from heterometallic MOF for syngas production by electrocatalytic reduction of CO_2 in water. *J. Solid State Chem.* **2018**, *263*, 44–51. [[CrossRef](#)]
87. Kim, N.-I.; Sa, Y.J.; Cho, S.-H.; So, I.; Kwon, K.; Joo, S.H.; Park, J.-Y. Enhancing Activity and Stability of Cobalt Oxide Electrocatalysts for the Oxygen Evolution Reaction via Transition Metal Doping. *J. Electrochem. Soc.* **2016**, *163*, F3020–F3028. [[CrossRef](#)]
88. Wang, G.; Shen, X.; Horvat, J.; Wang, B.; Liu, H.; Wexler, D.; Yao, J. Hydrothermal synthesis and optical, magnetic, and supercapacitance properties of nanoporous cobalt oxide nanorods. *J. Phys. Chem. C* **2009**, *113*, 4357–4361. [[CrossRef](#)]

89. Alvarez, A.; Ivanova, S.; Centeno, M.A.; Odriozola, J.A. Sub-ambient CO oxidation over mesoporous Co₃O₄: Effect of morphology on its reduction behavior and catalytic performance. *Appl. Catal. A Gen.* **2012**, *431–432*, 9–17. [[CrossRef](#)]
90. Tu, S.; Chen, Y.; Zhang, X.; Yao, J.; Wu, Y.; Wu, H.; Zhang, J.; Wang, J.; Mu, B.; Li, Z.; et al. Complete catalytic oxidation of formaldehyde at room temperature on Mn_xCo_{3-x}O₄ catalysts derived from metal-organic frameworks. *Appl. Catal. A Gen.* **2021**, *611*, 117975. [[CrossRef](#)]
91. Park, K.R.; Jeon, J.E.; Kim, K.; Oh, N.; Ko, Y.H.; Lee, J.; Lee, S.H.; Ryu, J.H.; Han, H.; Mhin, S. Synthesis of rod-type Co_{2.4}Mn_{0.6}O₄ via oxalate precipitation for water splitting catalysts. *Appl. Surf. Sci.* **2020**, *510*, 145390. [[CrossRef](#)]
92. Gautier, J.L.; Rios, E.; Gracia, M.; Marco, J.F.; Gancedo, J.R. Characterisation by X-ray photoelectron spectroscopy of thin Zn/Mn Co O 1 G x G 0 spinel films prepared by low-temperature spray x 3yx 4 pyrolysis. *Thin Solid Films* **1997**, *311*, 51–57. [[CrossRef](#)]
93. Tang, W.; Wang, S.; Xiao, W.; Du, S.; Lu, X.; Hoang, S.; Ding, J.; Gao, P.-X. Pre-surface leached cordierite honeycombs for Mn_xCo_{3-x}O₄ nano-sheet array integration with enhanced hydrocarbons combustion. *Catal. Today* **2019**, *320*, 196–203. [[CrossRef](#)]
94. Cullity, B.D.; Graham, C.D. *Introduction to Magnetic Materials*, 2nd ed.; IEEE: Piscataway, NJ, USA, 2008; Volume 59.
95. Xue, Z.; Liu, K.; Liu, Q.; Li, Y.; Li, M.; Su, C.-Y.; Ogiwara, N.; Kobayashi, H.; Kitagawa, H.; Liu, M.; et al. Missing-linker metal-organic frameworks for oxygen evolution reaction. *Nat. Commun.* **2019**, *10*, 5048. [[CrossRef](#)]
96. Shit, S.; Bolar, S.; Murmu, N.C.; Kuila, T. An account of the strategies to enhance the water splitting efficiency of noble-metal-free electrocatalysts. *J. Energy Chem.* **2021**, *59*, 160–190. [[CrossRef](#)]
97. Li, J.; Liang, X.; Xu, S.; Hao, J. Catalytic performance of manganese cobalt oxides on methane combustion at low temperature. *Appl. Catal. B Environ.* **2009**, *90*, 307–312. [[CrossRef](#)]
98. Menezes, P.W.; Indra, A.; Sahraie, R.; Bergmann, A. Cobalt–Manganese-Based Spinel as Multifunctional Materials that Unify Catalytic Water Oxidation and Oxygen Reduction Reactions. *ChemSusChem* **2015**, *8*, 164–171. [[CrossRef](#)]
99. Anne, R.; Acedera, E.; Gupta, G.; Mamlouk, M.; Donnabelle, M.; Balela, L. Solution combustion synthesis of porous Co₃O₄ nanoparticles as oxygen evolution reaction (OER) electrocatalysts in alkaline medium. *J. Alloys Compd.* **2020**, *836*, 154919. [[CrossRef](#)]
100. Yu, Y.; Zhang, J.; Zhong, M.; Guo, S. Co₃O₄ Nanosheet Arrays on Ni Foam as Electrocatalyst for Oxygen Evolution Reaction. *Electrocatalysis* **2018**, *9*, 653–661. [[CrossRef](#)]
101. Menezes, P.W.; Indra, A.; Gutkin, V.; Driess, M. Boosting electrochemical water oxidation through replacement of Oh Co sites in cobalt oxide spinel with manganese. *Chem. Commun.* **2017**, *53*, 8018–8021. [[CrossRef](#)]
102. Alqahtani, D.M.; Zequine, C.; Ranaweera, C.; Siam, K.; Kahol, P.K.; Poudel, T.P.; Mishra, S.; Gupta, R.K. Effect of metal ion substitution on electrochemical properties of cobalt oxide. *J. Alloys Compd.* **2019**, *771*, 951–959. [[CrossRef](#)]
103. Ma, Y.; Zha, M.; Dong, Y.; Li, L.; Hu, G. Mn-doped Co₃O₄ nanoarrays as a promising electrocatalyst for oxygen evolution reaction Mn-doped Co₃O₄ nanoarrays as a promising electrocatalyst for oxygen evolution reaction. *Mater. Res. Express* **2019**, *6*, 115033. [[CrossRef](#)]
104. Wang, W.; Kuai, L.; Cao, W.; Huttula, M.; Ollikkala, S.; Ahopelto, T.; Honkanen, A.-P.; Huotari, S.; Yu, M.; Geng, B. Mass-production of Mesoporous MnCo₂O₄ Spinel with MnIV- and CoII-rich Surface for Superior Bifunctional Oxygen Electrocatalysis. *Angew. Chem. Int. Ed.* **2017**, *47*, 14977–14981. [[CrossRef](#)]
105. Natarajan, S.; Anantharaj, S.; Tayade, R.J.; Bajaj, H.C.; Kundu, S. Recovered Spinel MnCo₂O₄ from Spent Lithium Ion Batteries for Enhanced Electrocatalytic Oxygen Evolution in Alkaline Medium. *Dalton Trans.* **2017**, *46*, 14382–14392. [[CrossRef](#)]
106. Yan, D.; Li, Y.; Huo, J.; Chen, R.; Dai, L.; Wang, S. Defect Chemistry of Nonprecious-Metal Electrocatalysts for Oxygen Reactions. *Adv. Mater.* **2017**, *29*, 1606459. [[CrossRef](#)] [[PubMed](#)]
107. Cai, Z.; Bi, Y.; Hu, E.; Liu, W.; Dwarica, N.; Tian, Y.; Li, X.; Kuang, Y.; Li, Y.; Yang, X.; et al. Single-Crystalline Ultrathin Co₃O₄ Nanosheets with Massive Vacancy Defects for Enhanced Electrocatalysis. *Adv. Energy Mater.* **2018**, *8*, 1701694. [[CrossRef](#)]
108. Zhang, W.; Li, M.; Wang, X.; Zhang, X.; Niu, X.; Zhu, Y. Boosting catalytic toluene combustion over Mn doped Co₃O₄ spinel catalysts: Improved mobility of surface oxygen due to formation of Mn-O-Co bonds. *Appl. Surf. Sci.* **2022**, *590*, 153140. [[CrossRef](#)]
109. Qin, C.; Wang, B.; Wang, Y. Metal-organic frameworks-derived Mn-doped Co₃O₄ porous nanosheets and enhanced CO sensing performance. *Sens. Actuators B Chem.* **2022**, *351*, 130943. [[CrossRef](#)]
110. Biswas, S.; Dutta, B.; Mannodi-Kanakkithodi, A.; Clarke, R.; Song, W.; Ramprasad, R.; Suib, S.L. Heterogeneous mesoporous manganese/cobalt oxide catalysts for selective oxidation of 5-hydroxymethylfurfural to 2,5-diformylfuran. *Chem. Commun.* **2017**, *53*, 11751–11754. [[CrossRef](#)]
111. Hamdani, M.; Singh, R.N.; Chartier, P. Co₃O₄ and Co-Based Spinel Oxides Bifunctional Oxygen Electrodes. *Int. J. Electrochem. Sci.* **2010**, *5*, 556–577.
112. Bockris, J.O.M.; Otagawa, T. Mechanism of oxygen evolution on perovskites. *J. Phys. Chem.* **1983**, *87*, 2960–2971. [[CrossRef](#)]
113. Li, G.; Anderson, L.; Chen, Y.; Pan, M.; Chuang, P.-Y.A. New insights into evaluating catalyst activity and stability of oxygen evolution reactions in alkaline media. *Sustain. Energy Fuels* **2018**, *2*, 237–251. [[CrossRef](#)]
114. Indra, A.; Menezes, P.W.; Zaharieva, I.; Baktash, E.; Pfrommer, J.; Schwarze, M.; Dau, H.; Driess, M. Active mixed-valent MnO_x water oxidation catalysts through partial oxidation (corrosion) of nanostructured MnO particles. *Angew. Chem.-Int. Ed.* **2013**, *52*, 13206–13210. [[CrossRef](#)]
115. Zeng, K.; Li, W.; Zhou, Y.; Sun, Z.; Lu, C.; Yan, J.; Choi, J.-H.; Yang, R. Multilayer hollow MnCo₂O₄ microsphere with oxygen vacancies as efficient electrocatalyst for oxygen evolution reaction. *Chem. Eng. J.* **2021**, *421*, 127831. [[CrossRef](#)]

116. Fan, C.; Wu, X.; Li, M.; Wang, X.; Zhu, Y.; Fu, G.; Ma, T.; Tang, Y. Surface chemical reconstruction of hierarchical hollow inverse-spinel manganese cobalt oxide boosting oxygen evolution reaction. *Chem. Eng. J.* **2022**, *431*, 133829. [[CrossRef](#)]
117. Zhang, L.; Shi, L.; Huang, L.; Zhang, J.; Gao, R.; Zhang, D. Rational Design of High-Performance DeNO_x Catalysts Based on Mn_xCo_{3-x}O₄ Nanocages Derived from Metal–Organic Frameworks. *ACS Catal.* **2014**, *4*, 1753–1763. [[CrossRef](#)]
118. Lyons, M.E.G.; Brandon, M.P. The significance of electrochemical impedance spectra recorded during active oxygen evolution for oxide covered Ni, Co and Fe electrodes in alkaline solution. *J. Electroanal. Chem.* **2009**, *631*, 62–70. [[CrossRef](#)]
119. Silva, V.D.; Raimundo, R.A.; Simões, T.A.; Loureiro, F.J.; Fagg, D.P.; Morales, M.A.; Macedo, D.A.; Medeiros, E.S. ScienceDirect Nonwoven Ni e NiO/carbon fibers for electrochemical water oxidation. *Int. J. Hydrogen Energy* **2020**, *46*, 3798–3810. [[CrossRef](#)]
120. Silva, T.; Silva, V.; Santos, J.; Simões, T.; Macedo, D. Effect of Cu-doping on the activity of calcium cobaltite for oxygen evolution reaction. *Mater. Lett.* **2021**, *298*, 130026. [[CrossRef](#)]
121. Silva, V.D.; Simões, T.A.; Loureiro, F.J.; Fagg, D.P.; Figueiredo, F.M.; Medeiros, E.S.; Macedo, D.A. Solution blow spun nickel oxide/carbon nanocomposite hollow fibres as an efficient oxygen evolution reaction electrocatalyst. *Int. J. Hydrogen Energy* **2019**, *44*, 14877–14888. [[CrossRef](#)]